

Shearing-box simulations of MRI-driven turbulence in weakly collisional accretion discs

Philipp Kempfski,¹[★] Eliot Quataert,¹ Jonathan Squire,² Matthew W. Kunz^{3,4}

¹*Department of Astronomy and Theoretical Astrophysics Center, University of California, Berkeley, Berkeley, CA 94720, USA*

²*Department of Physics, University of Otago, 730 Cumberland St, North Dunedin, Dunedin 9016, New Zealand*

³*Department of Astrophysical Sciences, Princeton University, 4 Ivy Lane, Princeton, New Jersey 08544, USA*

⁴*Princeton Plasma Physics Laboratory, PO Box 451, Princeton, New Jersey 08543, USA*

Accepted XXX. Received YYY; in original form ZZZ

ABSTRACT

We present a systematic shearing-box investigation of MRI-driven turbulence in a weakly collisional plasma by including the effects of an anisotropic pressure stress, i.e. anisotropic (Braginskii) viscosity. We constrain the pressure anisotropy (Δp) to lie within the stability bounds that would be otherwise imposed by kinetic microinstabilities. We explore a broad region of parameter space by considering different Reynolds numbers and magnetic-field configurations, including net vertical flux, net toroidal-vertical flux and zero net flux. Remarkably, we find that the level of turbulence and angular-momentum transport are not greatly affected by large anisotropic viscosities: the Maxwell and Reynolds stresses do not differ much from the MHD result. Angular-momentum transport in Braginskii MHD still depends strongly on *isotropic* dissipation, e.g., the isotropic magnetic Prandtl number, even when the anisotropic viscosity is orders of magnitude larger than the isotropic diffusivities. Braginskii viscosity nevertheless changes the flow structure, rearranging the turbulence to largely counter the parallel rate of strain from the background shear. We also show that the volume-averaged pressure anisotropy and anisotropic viscous transport decrease with increasing isotropic Reynolds number (Re); e.g., in simulations with net vertical field, the ratio of anisotropic to Maxwell stress (α_A/α_M) decreases from ~ 0.5 to ~ 0.1 as we move from $\text{Re} \sim 10^3$ to $\text{Re} \sim 10^4$, while $\langle 4\pi\Delta p/B^2 \rangle \rightarrow 0$. Anisotropic transport may thus become negligible at high Re . Anisotropic viscosity nevertheless becomes the dominant source of heating at large Re , accounting for $\gtrsim 50\%$ of the plasma heating. We conclude by briefly discussing the implications of our results for RIAFs onto black holes.

Key words: accretion discs – instabilities – MHD – plasmas – turbulence

1 INTRODUCTION

Magnetohydrodynamic (MHD) turbulence driven by the magnetorotational instability (MRI; Balbus & Hawley 1991) is widely considered to be one of the key engines powering angular-momentum transport in accretion discs. As a result, the growth of the MRI and the subsequent MHD turbulence it produces have been studied extensively over the years (see e.g. Hawley et al. 1995; Balbus & Hawley 1998; Hawley et al. 2001).

One uncertainty in the application of the MRI is that the MHD fluid approximation is not well justified in a number of astrophysical systems. This includes radiatively inefficient accretion flows (RIAFs), in which the Coulomb mean

free path is larger than the typical system size (Mahadevan & Quataert 1997). Departures from the ideal-MHD framework are therefore required and at first glance it may seem necessary to model the system as a fully collisionless plasma in six-dimensional phase space. The goal of this paper is to better understand the nonlinear evolution of the MRI under such conditions.

While it has recently become possible to run kinetic simulations of the MRI using particle-in-cell codes (Riquelme et al. 2015; Hoshino 2015; Kunz et al. 2016; Inchingolo et al. 2018), such simulations remain far too expensive (at least in three dimensions) to explore parameter space. However, a variety of recent theory (Schekochihin et al. 2008; Kunz et al. 2014; Sironi & Narayan 2015; Riquelme et al. 2015) suggests that ion-Larmor scale kinetic instabilities such as the mirror and firehose instabilities, which grow readily in low collision-

[★] E-mail: philipp.kempfski@berkeley.edu

ality, weakly magnetized plasmas, act to increase the effective collision rate via wave-particle interactions. This result is of great utility, as it at least partially motivates modeling the system as a weakly collisional plasma. The advantage of this framework is that non-ideal effects are simply introduced as additional terms in the ideal fluid equations, which is much simpler than evolving a six-dimensional distribution function of the plasma particles.

The linear growth of the MRI differs from its ideal-MHD counterpart in both a collisionless (Quataert et al. 2002) and a weakly collisional (Balbus 2004) plasma. However, despite some work with simplified fluid models and kinetic simulations, we lack detailed understanding of how kinetic physics affects the saturated MRI turbulence. Some insight has been gained by the work of Squire et al. (2017a), who focused on the nonlinear growth phase of the MRI in high- β low-collisionality plasmas. They argued that due to the onset of the aforementioned microinstabilities, the nonlinear growth phase of the kinetic MRI (KMRI) always returns to MHD-like evolution. Similarly, the saturation into turbulence appeared to be unaffected by non-ideal physics. These results provided insight into the physics behind earlier work on collisionless accretion discs by Sharma et al. (2006), who found that the properties of KMRI-induced turbulence were not too different from MHD. This resemblance has also been found in global general-relativistic simulations (Foucart et al. 2016; Foucart et al. 2017), which employed an extended-MHD framework with anisotropic viscosity and conductivity.

In this paper, we carry out a systematic shearing-box study of MRI-induced turbulence in a low-collisionality plasma with explicit resistivity and viscosity. To model non-ideal effects we use Braginskii’s closure for magnetized, weakly collisional plasmas (Braginskii 1965), commonly referred to as “Braginskii MHD”. As explained below, the anisotropic viscosity in Braginskii’s closure is equivalent to including an anisotropic pressure stress in the MHD equations. The closure is the simplest, well motivated model to capture key aspects of kinetic physics on large scales.

There are a number of questions that motivate such a parameter exploration. Perhaps most importantly, it will clarify the relevance of non-ideal physics for angular-momentum transport and plasma heating, including the additional contribution to the total stress tensor that comes directly from the pressure anisotropy.

While the Maxwell and Reynolds stresses have been studied extensively in MHD, significantly less is known about the non-ideal, anisotropic viscous stress. Most simulations to date found that its contribution to angular-momentum transport is smaller than, but comparable to, the Maxwell stress. However, given that the pressure anisotropy is driven by gradients in the velocity field, we may expect isotropic dissipation to influence the anisotropic transport. It is therefore instructive to look at the relationship between anisotropic stress and the dimensionless isotropic Reynolds numbers.

Exploring a range of isotropic viscosities and resistivities is vital for a second reason. One of the most striking results of previous work on MRI-generated turbulence is the dependence on isotropic dissipation. Lesur & Longaretti (2007) and Fromang et al. (2007) showed that the MRI saturation amplitude is very sensitive to the choice of viscos-

ity and resistivity, with a particularly strong dependence on their ratio, the magnetic Prandtl number. It is plausible to speculate that an additional large anisotropic viscosity may alter the effective Prandtl number. This claim is further motivated by the kinetic MRI simulations of Kunz et al. (2016), who showed that a high- β collisionless plasma behaved in some ways like a high-magnetic-Prandtl-number fluid. It is therefore unclear to what extent we should expect to recover the usual Prandtl-number dependence in Braginskii MHD.

Another important factor to consider is how the very building blocks of MHD turbulence are modified in low-collisionality plasmas and whether this may change the large-scale turbulent state in low-collisionality accretion discs. Squire et al. (2016) and Squire et al. (2017b) showed that collisionless and weakly collisional plasmas cannot support linearly polarized shear-Alfvén waves above a critical amplitude due to a cancellation between the Lorentz force and the anisotropic-pressure force. It is unclear if and how this might affect the large-scale turbulent properties in accretion discs.

The layout of this paper is as follows. In Section 2 we discuss the method and setup for our study of turbulence in Braginskii MHD. The main focus is on boxes threaded by a net vertical magnetic field, with the corresponding results described in Section 3. We consider other initial field configurations in Section 4. Finally, Section 5 summarizes our key results and discusses current limitations and future directions.

2 METHOD

2.1 Equations

We use the pseudo-spectral code SNOOPY (Lesur & Longaretti 2007) to evolve the incompressible MHD equations with anisotropic pressure in a shearing box:

$$\nabla \cdot \mathbf{U} = 0, \quad (1)$$

$$\begin{aligned} \frac{D\mathbf{U}}{Dt} = & -2\Omega \times \mathbf{U} + 2\Omega S x \hat{\mathbf{x}} - \nabla \left(p_{\perp} + \frac{B^2}{8\pi} \right) \\ & + \nabla \cdot \left[\hat{\mathbf{b}} \hat{\mathbf{b}} \left(\frac{B^2}{4\pi} + \Delta p \right) \right] + \nu \nabla^2 \mathbf{U}, \end{aligned} \quad (2)$$

$$\frac{D\mathbf{B}}{Dt} = \mathbf{B} \cdot \nabla \mathbf{U} + \eta \nabla^2 \mathbf{B}, \quad (3)$$

where $\hat{\mathbf{b}} = \mathbf{B}/B$ is the unit vector along the magnetic field \mathbf{B} and the density has been set to unity. Because our model is incompressible, we choose p_{\perp} at each timestep so as to satisfy $\nabla \cdot \mathbf{U} = 0$. We include an explicit isotropic viscosity ν and resistivity η . The velocity field \mathbf{U} consists of a background shear \mathbf{U}_0 and perturbations \mathbf{u} : $\mathbf{U} = \mathbf{U}_0 + \mathbf{u}$. We adopt an equilibrium Keplerian background profile $\mathbf{U}_0 = -Sx\hat{\mathbf{y}}$, with $S = \frac{3}{2}\Omega$, and we use the code to compute the evolution of \mathbf{u} and \mathbf{B} . We use the 2/3 de-aliasing rule to prevent spurious modes originating from the nonlinear terms in (1)–(3).

At any timestep, the pressure anisotropy Δp entering the momentum equation (2) is calculated via:

$$\Delta p = p_{\perp} - p_{\parallel} = 3\mu_B \hat{\mathbf{b}} \hat{\mathbf{b}} : \nabla \mathbf{U}, \quad (4)$$

where p_{\perp} and p_{\parallel} are the thermal pressures in the directions perpendicular and parallel to the local magnetic field

(Braginskii 1965). Equation (4) can be obtained from the kinetic evolution equations of the plasma (Chew et al. 1956; Kulsrud 1983; Schekochihin et al. 2010) in the weakly collisional regime $v_c/|\nabla \mathbf{u}| \gg 1$, where v_c is the collision rate of the plasma. In equation (4) we also assume that the effect of heat fluxes on the pressure anisotropy can be neglected, an assumption that is formally valid when $v_c/|\nabla \mathbf{u}| \gg \beta^{1/2}$ (Mikhailovskii & Tsypin 1971), where $\beta = 8\pi p/B^2$ is the ratio of thermal to magnetic pressure (see Squire et al. 2017a for more discussion of the different regimes).

Upon substitution into (2), Δp can be shown to behave as a diffusion operator acting along $\hat{\mathbf{b}}$. Its role is therefore to damp the component of the velocity along the local magnetic field that has gradients along the local magnetic field. Due to its diffusive contribution, throughout this work we will refer to the coefficient μ_B as anisotropic (or Braginskii) viscosity.

2.2 Modeling Kinetic Microinstabilities

The background shear and MRI-induced magnetic-field growth naturally lead to a finite pressure anisotropy. However, once Δp becomes comparable to the magnetic pressure, plasma instabilities are excited that are not fully captured by the set of equations (1)–(3). The two main microinstabilities that need to be accounted for are the mirror instability (Barnes 1966; Hasegawa 1969), excited if

$$\Delta p \gtrsim \frac{B^2}{8\pi} \quad (5)$$

and the firehose instability (Rosenbluth 1956; Chandrasekhar et al. 1958; Parker 1958), which is excited when

$$\Delta p \lesssim -\frac{B^2}{4\pi}. \quad (6)$$

Wave-particle interactions induced by these instabilities increase the effective collisionality of the system, which in turn acts to isotropize the pressure tensor. As a result, the mirror/firehose instability, excited by a growing/declining pressure anisotropy, acts to halt further growth/decline. Kinetic simulations have shown that these instabilities tend to pin the anisotropy near the instability thresholds (Kunz et al. 2016).

We include this kinetic result by imposing hard-wall limits on Δp . If Δp is driven outside of the stability limits given by $-B^2/4\pi < \Delta p < B^2/8\pi$, then it is pinned to either $\Delta p = -B^2/4\pi$ or $\Delta p = B^2/8\pi$, depending on which boundary is crossed. Otherwise, Δp is determined by equation (4).

By using instantaneous bounds on Δp , we essentially assume that the only effect of microinstabilities is to halt the growth of Δp , with no direct change to other fluid quantities. For the firehose instability, this limiting behaviour arises due to particle scattering, while for the mirror instability, there is a long phase where small-scale magnetic fluctuations grow secularly in time. Although the limiter model can, in principle, capture the effect of either scattering or secular growth if we consider \mathbf{u} and \mathbf{B} in equations (1)–(3) to be large-scale averages, there may be other poorly understood effects that are not captured. In addition, the assumption that Δp limiters act instantaneously is incorrect for motions with timescales approaching the ion gyro time. Because we find that the cascade continues almost unaffected to scales well

below the Braginskii viscous scale, this could mean that the smallest-scale motions will be more strongly affected by Δp forces than we assume here. It is unclear if and how these additional effects could be incorporated in a fluid model, and a kinetic description is likely necessary to fully capture all the underlying physics (see Schekochihin et al. 2008, Kunz et al. 2014, Squire et al. 2017a for more discussion).

We have also run two simulations without limiters at the firehose instability threshold. These no-firehose-limiter simulations are partially justified by the fact that the parallel firehose instability is already present in the Braginskii equations (by contrast, the mirror instability is not). However, the kinetic simulations in Kunz et al. (2014) showed that the oblique firehose instability is probably more important for maintaining Δp near the instability threshold. For this reason, most of our simulations have both firehose and mirror limiters included.

2.3 Setup

Throughout this work we set $\Omega = 1$. Since we want to explore any pressure-anisotropy-induced differences, for every Braginskii MHD simulation we also carry out a corresponding MHD simulation in which $\Delta p = 0$. Given the sensitivity of MRI turbulence to isotropic dissipation, we test a number of isotropic viscosities ν and resistivities η . We define the associated dimensionless Reynolds number,

$$\text{Re} = \frac{SL_z^2}{\nu}; \quad (7)$$

the magnetic Reynolds number,

$$\text{Re}_M = \frac{SL_z^2}{\eta}; \quad (8)$$

and their ratio, the magnetic Prandtl number,

$$\text{Pm} = \frac{\nu}{\eta}. \quad (9)$$

We also define the analogous Braginskii Reynolds number,

$$\text{Re}_B = \frac{SL_z^2}{\mu_B}. \quad (10)$$

To quantify the turbulent angular-momentum transport, we define the dimensionless transport coefficient

$$\alpha = \alpha_{\text{Re}} + \alpha_{\text{M}} + \alpha_{\text{A}}, \quad (11)$$

where

$$\alpha_{\text{Re}} = \langle v_x v_y \rangle / (S^2 L_z^2), \quad (12)$$

$$\alpha_{\text{M}} = -\left\langle \frac{B_x B_y}{4\pi} \right\rangle / (S^2 L_z^2), \quad (13)$$

$$\alpha_{\text{A}} = -\left\langle \frac{\Delta p}{B^2} B_x B_y \right\rangle / (S^2 L_z^2) \quad (14)$$

are the contributions from the volume-averaged ($\langle \dots \rangle$) Reynolds stress, Maxwell stress and anisotropic viscous stress respectively, normalized by $S^2 L_z^2$. This is the incompressible version of the compressible transport parameter, which is usually normalized using the initial pressure (see e.g. Hawley et al. 1995; Sharma et al. 2006). While α_{M} and

α_{Re} are present both in ordinary MHD and in Braginskii MHD, α_A requires a pressure anisotropy and is therefore only nonzero in Braginskii MHD.

To capture the most important parasitic modes that break up the MRI “channel” modes into turbulence, most of our simulations are in horizontally elongated boxes of size $L_x = 4$, $L_y = 4$ and $L_z = 1$ (Bodo et al. 2008; Pessah & Goodman 2009; Longaretti & Lesur 2010). However, we did also explore other aspect ratios. We find that Braginskii MHD results are particularly sensitive to box size, with dramatically different results in horizontally narrow boxes with net vertical flux (see Appendix A1).

In order to satisfy the Courant condition at large μ_B , we are limited to rather modest resolutions by current standards, despite sub-cycling over the Δp term in equation (2) in simulations with large μ_B (where we used 5 or 8 as the maximum number of sub-cycles per main MHD timestep). Most of our full simulations in $4 \times 4 \times 1$ boxes have resolution $256 \times 128 \times 64$. To test very large μ_B , we also ran a number of lower resolution simulations. In each case, the initial magnetic field and background shear are perturbed with small-amplitude white noise.

The isotropic viscosities and resistivities are chosen such that the dissipative scales are properly resolved. This places an upper bound on the Re and Re_M that we can explore in a full Braginskii simulation, given the attainable resolutions. To explore the relationship between anisotropic stress and the isotropic diffusivities, ideally we would like to cover a broad range of viscosities and resistivities, and explore the limit $\text{Re} \rightarrow \infty$, $\text{Re}_M \rightarrow \infty$ at fixed Pm . However, the required resolutions are computationally unfeasible with the numerical methods that we use here.

To test larger Reynolds numbers in higher resolution, we perform a number of “Composite” MHD–Braginskii MHD simulations. In these simulations, we first evolve the equations of MHD for a time $t\Omega = 100$. The turbulent MHD flow fields are then restarted with anisotropic viscosity included and evolved further for several Ω^{-1} . These composite simulations are motivated by our observation that anisotropic viscosity transforms MHD flow fields into Braginskii-like flow fields on timescales shorter than the orbital time. We have tested that, by restarting MHD turbulence with anisotropic viscosity, we are able to recover the typical Δp and α_A of the corresponding full Braginskii simulation in a fraction of Ω^{-1} . We show an example of this behavior in Appendix B.

This method offers insight into the statistics of Braginskii MHD turbulence at large Reynolds numbers, even when the Braginskii equations are evolved for a rather short amount of time. As a result, the composite simulations enable us to explore isotropic Reynolds numbers ($\text{Re} \sim 10^4$) and resolutions ($768 \times 384 \times 192$ and $384 \times 192 \times 96$) that are otherwise unattainable for a full Braginskii simulation with large μ_B .

We also perform a number of simulations in which the viscosity and resistivity are replaced by hyperdiffusion operators, $\nu_4 \nabla^4 \mathbf{U}$ and $\eta_4 \nabla^4 \mathbf{B}$. We define the associated dimensionless quantities $\text{Re}_4 = SL_z^4/\nu_4$ and $\text{Re}_{M,4} = SL_z^4/\eta_4$. Using hyperdiffusion serves as an alternative method to probe larger effective Reynolds numbers, by potentially increasing the size of the inertial range without increasing the resolution. The k^4 dependence of hyperdiffusion allows us to dissipate energy above the grid scale even for very small ν_4 , with-

out constraining the turbulence at intermediate wavenumbers, thus mimicking turbulence at somewhat larger Re than would be possible with standard diffusion operators (note, however, that the Re_4 defined above is *not* the effective Reynolds number of our hyperdiffusion simulations).

While our main focus is on simulation domains with a net vertical field (Section 3), we also discuss other initial magnetic-field configurations: net vertical and toroidal field (4.1), as well as zero net flux (4.2).

3 NET VERTICAL FIELD

The main part of our study concerns boxes initially threaded by a purely vertical magnetic field,

$$\langle \mathbf{B} \rangle = B_0 \hat{\mathbf{z}}. \quad (15)$$

We choose $B_0 = \sqrt{8\pi/1348} \Omega L_z$, so that the fastest-growing MRI mode in MHD has wavelength $\lambda_{\text{MRI}} = 0.25L_z$.

Table 1 gives a summary of our different choices of Re , Re_M and Re_B . The main result of this section concerns anisotropic stress and its dependence on the values of Re and Re_M . However, we postpone our discussion of this result until section 3.2 and first look at the overall Braginskii MHD evolution, and its similarities and differences relative to MHD.

3.1 Comparison to MHD

In each of our simulations the qualitative evolution follows the same pattern. The initial small-amplitude perturbations are amplified by the MRI. The amplification continues until the MRI modes reach large amplitudes and become unstable to parasitic instabilities (Goodman & Xu 1994). These are secondary instabilities that grow on the large field and flow gradients in the MRI mode, causing it to break up into turbulence. Squire et al. (2017a) argued that the dominant parasitic modes are not too different in Braginskii MHD. This is broadly consistent with our numerical results summarized below, although we do often see somewhat larger α in the Braginskii case during a short initial transient phase. In addition, we find a very significant box-size dependence in Braginskii MHD (see Appendix A1).

Figure 1 shows the evolution of the simulation with $\text{Re} = 1500$ and $\text{Pm} = 2$. The dotted lines track the MHD evolution, while the solid lines correspond to Braginskii MHD with $\text{Re}_B = 0.75$. The two models show similar behavior and the resultant turbulent energy densities and angular-momentum transport are close to identical. The main qualitative differences appear at early times, during the MRI growth phase. Braginskii viscosity delays the growth along the initial field direction ($\langle B_z^2 \rangle$ and $\langle v_z^2 \rangle$) through stronger damping of the initial white-noise perturbations. In addition, in the Braginskii MHD simulation the MRI is able to grow to larger amplitudes, before it eventually saturates.

For all of the cases we simulated, the transport is not greatly affected by the anisotropic viscosity. This includes our simulations with both limiters included, as well as our full simulation without a firehose limiter. The main difference is the presence of the anisotropic viscous stress. The Maxwell and Reynolds stresses are very similar in both MHD and Braginskii MHD.

Table 1. Summary of simulations with net vertical field. **Full simulations:** each simulation set at a fixed Re , Re_M consists of an MHD simulation (top) and Braginskii MHD simulation(s) (bottom). The transport coefficients α and the mean pressure anisotropies were averaged over $t\Omega = 100 - 200$. “Braginskii****” indicates a Braginskii MHD simulation without firehose limiter included. **Composite MHD–Braginskii MHD simulations:** MHD fields are restarted at $t\Omega = 100$ using Braginskii MHD. For simulations at resolution $384 \times 192 \times 96$, averages were taken over $t\Omega = 101 - 110$. For the simulations at higher resolution, averages are over $t\Omega = 101 - 102$. “Composite****” indicates a simulation where MHD flow fields were restarted in Braginskii MHD without firehose limiter.

Sim. Type	Resolution	Re	Re_M	Pm	Re_B	α_{Re}	α_M	α_A	α	$4\pi \langle \Delta p \rangle / \langle B^2 \rangle$	$\langle 4\pi \Delta p / B^2 \rangle$	α_A / α_M
Full MHD	(256, 128, 64)	6000	3000	0.5	–	0.0065	0.031	–	0.037	–	–	–
Full Braginskii	(256, 128, 64)	6000	3000	0.5	0.75	0.0084	0.031	0.0086	0.048	0.21	0.15	0.28
Full MHD	(256, 128, 64)	750	750	1	–	0.0051	0.020	–	0.025	–	–	–
Full Braginskii	(256, 128, 64)	750	750	1	0.75	0.0065	0.019	0.0090	0.035	0.41	0.30	0.47
Full MHD	(256, 128, 64)	4500	4500	1	–	0.0062	0.036	–	0.043	–	–	–
Full Braginskii	(256, 128, 64)	4500	4500	1	0.75	0.0097	0.044	0.011	0.065	0.19	0.12	0.25
Full MHD	(256, 128, 64)	1500	3000	2	–	0.0078	0.046	–	0.054	–	–	–
Full Braginskii	(256, 128, 64)	1500	3000	2	0.75	0.012	0.049	0.016	0.077	0.28	0.19	0.35
Full Braginskii****	(256, 128, 64)	1500	3000	2	0.75	0.011	0.045	0.016	0.072	-0.021	-22.3	0.36
Full MHD	(256, 128, 64)	750	6000	8	–	0.015	0.10	–	0.12	–	–	–
Full Braginskii	(256, 128, 64)	750	6000	8	0.75	0.022	0.11	0.031	0.17	0.21	0.13	0.27
Full MHD	(192, 96, 48)	1500	750	0.5	–	0.0047	0.015	–	0.019	–	–	–
Full Braginskii	(192, 96, 48)	1500	750	0.5	0.3	0.0049	0.014	0.0062	0.025	0.39	0.29	0.46
Full MHD	(192, 96, 48)	1500	3000	2	–	0.0082	0.049	–	0.057	–	–	–
Full Braginskii	(192, 96, 48)	1500	3000	2	300	0.0084	0.045	0.0006	0.054	0.012	0.032	0.013
Full Braginskii	(192, 96, 48)	1500	3000	2	75	0.0090	0.050	0.0020	0.061	0.037	0.069	0.044
Full Braginskii	(192, 96, 48)	1500	3000	2	15	0.0093	0.047	0.0065	0.063	0.12	0.14	0.15
Full Braginskii	(192, 96, 48)	1500	3000	2	3	0.011	0.047	0.013	0.071	0.23	0.18	0.29
Full Braginskii	(192, 96, 48)	1500	3000	2	0.3	0.0097	0.040	0.013	0.063	0.26	0.17	0.33
Full MHD	(128, 64, 32)	1500	3000	2	–	0.0069	0.036	–	0.043	–	–	–
Full Braginskii	(128, 64, 32)	1500	3000	2	0.075	0.011	0.047	0.013	0.072	0.21	0.13	0.29
Composite	(384, 192, 96)	750	750	1	0.75	0.0043	0.011	0.0055	0.021	0.42	0.31	0.49
Composite	(384, 192, 96)	3000	3000	1	0.75	0.0071	0.026	0.0090	0.042	0.28	0.19	0.35
Composite	(384, 192, 96)	10500	10500	1	0.75	0.011	0.057	0.011	0.078	0.12	0.060	0.19
Composite****	(384, 192, 96)	10500	10500	1	0.75	0.013	0.073	0.0079	0.094	-0.28	-17.7	0.11
Composite	(576, 288, 144)	10500	10500	1	0.75	0.014	0.068	0.013	0.095	0.13	0.070	0.19
Composite	(768, 384, 192)	21000	21000	1	0.75	0.010	0.081	0.0088	0.10	0.076	0.026	0.11
Composite	(768, 384, 192)	10500	42000	4	0.75	0.020	0.12	0.017	0.15	0.076	0.016	0.14

The remarkable similarities between the MHD and weakly collisional solutions draw us to an interesting conclusion: even with large anisotropic viscosity, the turbulent amplitudes are still set primarily by the isotropic Reynolds and magnetic Reynolds numbers. This is illustrated in Figure 2, where we show the time-averaged transport coefficients of the MHD (black) and Braginskii MHD (red) runs at different Pm . For the Braginskii runs we also plot the transport due to just the Reynolds and Maxwell stresses as empty red diamonds. The error bars shown in Figure 2 are estimates for the standard deviations of the average transport coefficients, which use a binning time of $t = 10\Omega^{-1}$ (due to the short Braginskii timesteps, our simulations were not evolved long enough for an error analysis similar to Lon-

garetti & Lesur 2010). Nevertheless, they illustrate that the $\alpha_{\text{Re}} + \alpha_M$ of the Braginskii calculation agrees well with MHD. In Braginskii MHD we recover the usual Prandtl-number dependence found in MHD, thus showing that turbulence is still strongly influenced by the isotropic diffusivities, even when $\text{Re}_B \ll \text{Re}$.

The result that angular-momentum transport is not significantly affected by large anisotropic viscosities is partly due to the anisotropic-pressure limiters. These limit Δp to being comparable to the local field strength, which implies that the anisotropic stress cannot become significantly larger than the Maxwell stress. However, we see here that the box-averaged anisotropic stress can be substantially smaller than the Maxwell stress (e.g., $\alpha_A = 0.25\alpha_M$ in the full Braginskii

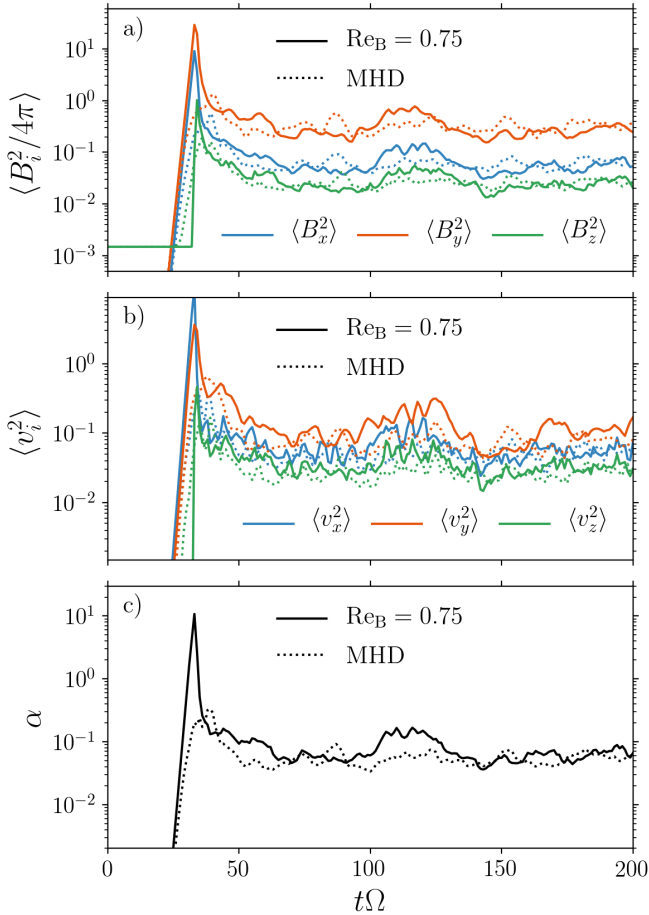


Figure 1. Evolution of energy densities and the transport coefficient α in simulations with $\text{Re} = 1500$ and $\text{Pm} = 2$ with net vertical flux. In the saturated phase the Braginskii model with $\text{Re}_B = 0.75$ (solid lines) closely matches MHD evolution (dotted lines).

run with $\text{Re} = 4500$ and $\text{Pm} = 1$; we also find that $\alpha_A \ll \alpha_M$ in high- Re composite simulations, as discussed in Section 3.2), which is less obvious, and surprising in light of previous results (e.g., Sharma et al. 2006 and Kunz et al. 2016, where α_A is comparable to α_M). Perhaps even more surprising is that we find little dependence of the angular-momentum transport on anisotropic viscosity even though the effective (Δp -limited) Braginskii viscosities considered here are much larger than the isotropic diffusivities. This is in contrast to the strong dependence of angular-momentum transport in a shearing box on isotropic diffusivities (Fromang et al. 2007; Lesur & Longaretti 2007). In addition, we show in Section 3.2 that angular-momentum transport is similar to MHD despite the fact that the flow structure in Braginskii MHD is quite different from MHD (e.g., Figure 9).

3.2 Anisotropic Transport in Braginskii MHD

In this section we explore aspects of angular-momentum transport that are specific to Braginskii MHD. Having demonstrated that the Maxwell and Reynolds stresses tend to track their values in the complementary MHD simula-

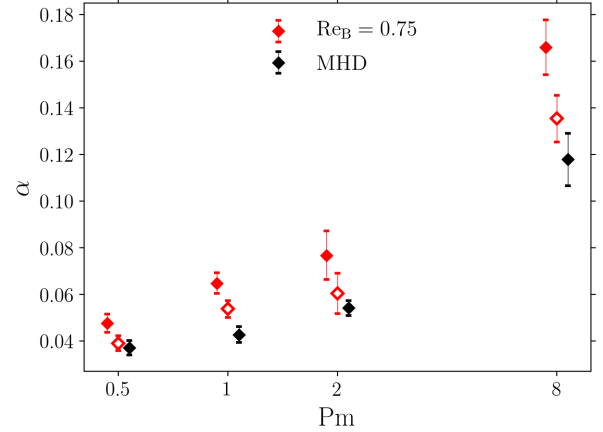


Figure 2. Temporal average of α for different Pm in MHD (black) and Braginskii MHD with $\text{Re}_B = 0.75$ (red). The filled diamonds represent the total transport coefficient α . The empty red diamonds count the contribution from $\alpha_{\text{Re}} + \alpha_M$ in the Braginskii simulation. The error bars are the standard deviations of the time-averaged α . The Maxwell and Reynolds stresses in Braginskii MHD show the usual MHD-like Prandtl-number dependence; the difference between MHD and Braginskii MHD is caused primarily by anisotropic stress. The $\text{Pm} = 0.5$ and $\text{Pm} = 2$ simulations have $\text{Re}_M = 3000$, the $\text{Pm} = 1$ simulation has $\text{Re}_M = 4500$ and $\text{Pm} = 8$ has $\text{Re}_M = 6000$. The points at a fixed Pm have been slightly displaced for visualization purposes.

tions, our main focus is on the evolution of the anisotropic stress and pressure anisotropy.

In Figure 3a we show the evolution of the Maxwell, Reynolds and anisotropic viscous stresses for the simulation with $\text{Re} = 1500$, $\text{Pm} = 2$ and $\text{Re}_B = 0.75$. The overall transport is dominated by the Maxwell stress, followed by the anisotropic and Reynolds stresses. This is similar to the results of the kinetic MRI simulations in Kunz et al. (2016) and the global extended-MHD simulation in Foucart et al. (2017). In all of our simulations we find that the Maxwell stress dominates.

Figure 3b shows the evolution of the box-averaged pressure anisotropy. In the initial growth phase of the MRI, Δp grows steadily until all cells are pinned at the mirror boundary. In the turbulent phase it then shows small oscillations around a roughly constant value. The background coloring shows the underlying $4\pi\Delta p/B^2$ distribution of cells over time. The inset shows this distribution across the simulation domain at a selected time ($t\Omega = 150$). Most cells are pinned at the microinstability limits, the majority being on the mirror side, giving an overall positive pressure anisotropy.

Figure 3c shows the evolution of heating due to isotropic and anisotropic diffusion, normalized by the total dissipation,

$$D = D_\eta + D_\nu + D_{\mu_B}, \quad (16)$$

where D_η is the resistive heating,

$$D_\eta = -\frac{\eta}{4\pi} \int d^3x \mathbf{B} \cdot \nabla^2 \mathbf{B}, \quad (17)$$

D_ν is the isotropic viscous heating,

$$D_\nu = -\nu \int d^3x \mathbf{u} \cdot \nabla^2 \mathbf{u}, \quad (18)$$

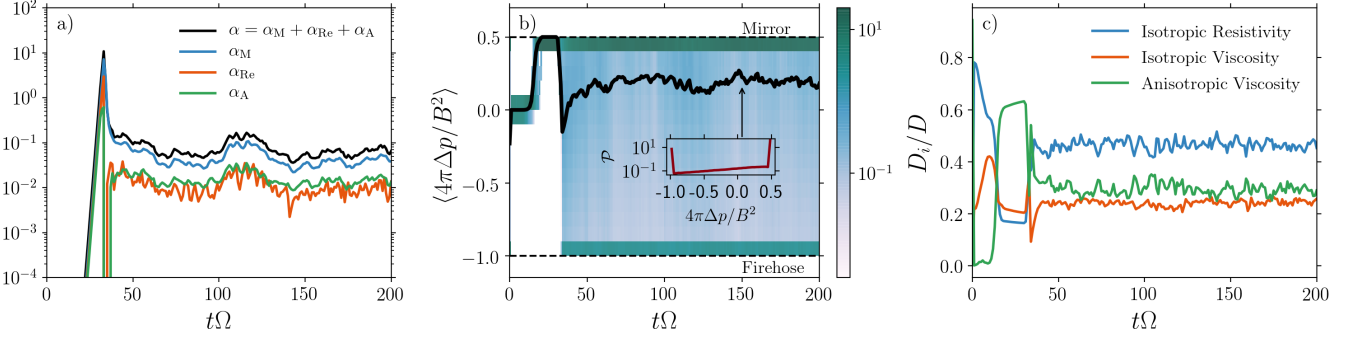


Figure 3. Braginskii MHD evolution for $\text{Re} = 1500$, $\text{Pm} = 2$ and $\text{Re}_B = 0.75$. **Panel a):** Evolution of the Maxwell (blue), Reynolds (orange), anisotropic (green) and total (black) transport coefficients in Braginskii MHD. **Panel b):** Evolution of the volume-averaged pressure anisotropy divided by (twice) the magnetic energy (black solid line). The background shading shows the underlying distribution of $4\pi\Delta p/B^2$ over time, showing that the majority of cells lie on the mirror boundary (the width of the region near the mirror and firehose boundaries is exaggerated for visualization purposes). The inset shows this distribution across the simulation domain at the time $t\Omega = 150$. **Panel c):** heating fractions of isotropic and anisotropic diffusivities over time. The heating is dominated by resistive heating (eq. 17), followed by anisotropic (eq. 19) and isotropic (eq. 18) viscous heating. See Figures 10 – 11 for how these results depend on Re .

and D_{μ_B} is the anisotropic viscous heating,

$$D_{\mu_B} = \int d^3x \Delta p \hat{\mathbf{b}}\hat{\mathbf{b}} : \nabla \mathbf{U}. \quad (19)$$

The pressure anisotropy Δp in equation (19) is computed with mirror and firehose limiters included. In this simulation with $\text{Re} = 1500$, $\text{Pm} = 2$ and $\text{Re}_B = 0.75$, resistive heating dominates, followed by anisotropic viscous heating and isotropic viscous heating.

3.2.1 Dependence on Re_B

One might expect that anisotropic viscous transport and anisotropic viscous heating will depend primarily on our choice of anisotropic viscosity μ_B . We show the dependence on Braginskii Reynolds number for simulations with $\text{Re} = 1500$ and $\text{Pm} = 2$ in Figure 4. Figure 4a shows that α_A/α_M increases with increasing anisotropic viscosity at large Re_B , reaching a plateau at small Re_B . Figure 4b shows the dependence of the time-averaged heating fractions on Re_B . D_{μ_B}/D has a dependence similar to α_A/α_M , increasing with increasing μ_B at large Re_B and approaching an approximately constant value at small Re_B . This is qualitatively similar to the results found by Squire et al. (2018) for strong Alfvénic turbulence. Note, however, that the final values of α_A/α_M and D_{μ_B}/D , reached at $\text{Re}_B \lesssim 1$, depend on Re and Re_M (see Figures 10 and 11).

The plateaus in Figure 4 at small Re_B (high μ_B) are related to the fact that, due to the presence of limiters, the effective μ_B saturates. Anisotropic transport and heating are most sensitive to the choice of anisotropic viscosity at small μ_B , when most fluid cells have Δp within the microinstability limits (eq. 5 & 6). But once μ_B is sufficiently large such that most cells lie outside of the limiter region, α_A/α_M and D_{μ_B}/D reach a plateau. We illustrate this in Figure 5a, where we show the distributions of $3\mu_B\hat{\mathbf{b}}\hat{\mathbf{b}} : \nabla \mathbf{U}4\pi/B^2$ for the different choices of Re_B . This is the pre-limiter Δp distribution divided by (twice) the magnetic energy, before any hard-wall limits are applied to Δp (the distribution with limiters is shown in the inset of Figure 3b). The anisotropic stress and

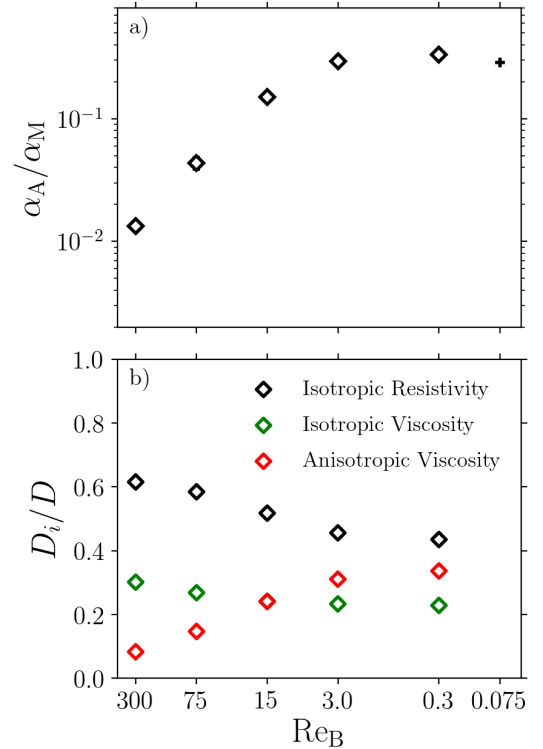


Figure 4. Dependence on Braginskii Reynolds number Re_B in simulations with $\text{Re} = 1500$, $\text{Pm} = 2$ at resolution $192 \times 96 \times 48$. **Panel a):** ratio of anisotropic to Maxwell stress, α_A/α_M , as a function of Braginskii Reynolds number. The black “+” is our largest- μ_B test, performed at lower resolution ($128 \times 64 \times 32$). Error bars are plotted, but not visible, as they are smaller than the marker size. **Panel b):** temporal averages of heating fractions of isotropic and anisotropic diffusivities, as a function of Re_B . Anisotropic viscous heating increases with decreasing Re_B , until it becomes approximately constant at large anisotropic viscosities. The simulation with $\text{Re}_B = 0.075$ at lower resolution is not shown, as it is uncertain whether the low resolution permits an accurate calculation of isotropic dissipation.

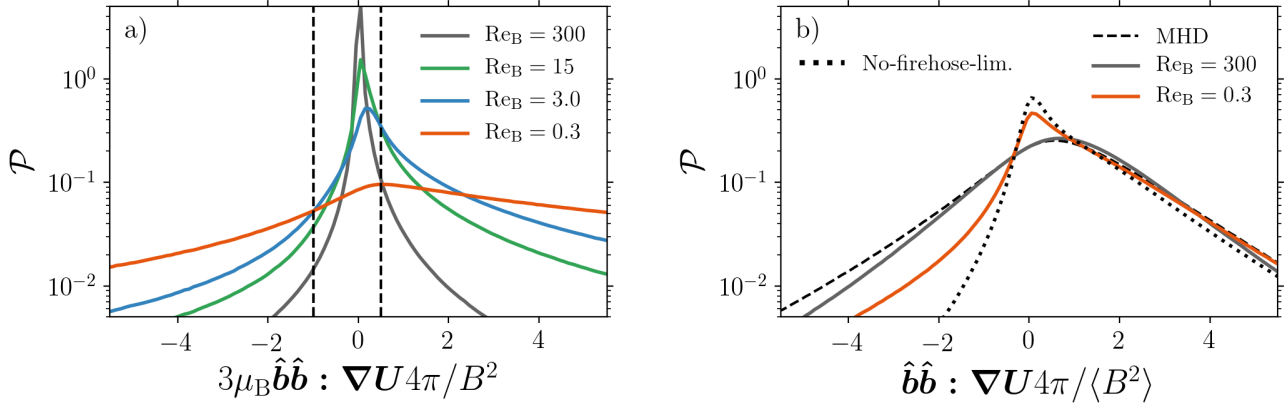


Figure 5. Distributions for the simulations summarized in Figure 4. **Panel a):** The pre-limiter distributions of $4\pi\Delta p/B^2$ for different Re_B . The dashed vertical lines denote the firehose (left) and mirror (right) limits. α_A/α_M reaches a plateau when the distribution of $3\mu_B \hat{b}\hat{b} : \nabla U 4\pi / B^2$ (before limiters are applied) becomes wide compared to the hard-wall limits. **Panel b):** At small Re_B there is a narrower distribution of $\hat{b}\hat{b} : \nabla U 4\pi / \langle B^2 \rangle$. The dotted line is our no-firehose-limiter simulation with $Re = 1500$, $Pm = 2$ and $Re_B = 0.75$, in which large negative $\hat{b}\hat{b} : \nabla U$ is even more suppressed (the distribution for $Re_B = 0.75$ with firehose limiter included is very similar to the $Re_B = 0.3$ distribution). These results are a consequence of anisotropic viscosity causing the turbulence to resist field-line stretching, i.e. $\hat{b}\hat{b} : \nabla U$ is minimized.

anisotropic heating fraction reach an almost constant value once the pressure anisotropy distribution lies mostly outside of the dashed vertical lines denoting the mirror and firehose limits. We find that typically $Re_B \lesssim 3$ is enough to approach the asymptotic value. This can be explained as follows: the presence of limiters causes the effective μ_B to saturate when $3\mu_B \hat{b}\hat{b} : \nabla U_0 = -3\mu_B b_x b_y S \sim B^2/4\pi$, or equivalently when $Re_B \sim 4\pi S^2 L_z^2 / B^2$. This gives $Re_B \sim$ a few for typical turbulent energy densities, which explains the plateaus in Figure 4.

Figure 5b shows that while the $3\mu_B \hat{b}\hat{b} : \nabla U 4\pi / B^2$ distribution becomes broader, the distribution of $\hat{b}\hat{b} : \nabla U 4\pi / \langle B^2 \rangle$ becomes narrower with increasing μ_B . In addition, large negative $\hat{b}\hat{b} : \nabla U$ is more suppressed in simulations without firehose limiter. This can be explained by the work of Squire et al. (2018), who demonstrated that anisotropic viscosity acts to minimize field-line stretching $\hat{b}\hat{b} : \nabla U$ to resist changes in magnetic-field strength and make the flow “magneto-immutable”.

3.2.2 Dependence on Re and Re_M : composite simulations

Is isotropic dissipation important for the level of anisotropic transport? It is well known that the Maxwell and Reynolds stresses show a strong dependence on isotropic viscosity and resistivity. Given the interdependence of the pressure anisotropy and velocity-field gradients, it is plausible that α_A will also be sensitive to the choice of isotropic Reynolds numbers. Our fully evolved Braginskii simulations (Table 1) tentatively suggest that the relative importance of α_A is greater at low Re and Re_M . This is best seen from the two simulations with $Pm = 1$: α_A/α_M decreases from 0.47 for $Re = 750$ to 0.25 for $Re = 4500$, a change significantly larger than the characteristic temporal fluctuations. To explore this dependence in detail and cover a broad range of viscosities and resistivities, we first make use of our composite MHD–Braginskii MHD simulations (see Section 2.3) and then simulations with hyperdiffusion.

Our composite simulations are summarized in the bottom part of Table 1. While we focus on simulations with $Pm = 1$, we also include a simulation with a larger Prandtl number, for which we used $Re = 10500$, $Re_M = 42000$. The presented values of $4\pi\langle\Delta p\rangle/\langle B^2\rangle$, $\langle 4\pi\Delta p/B^2 \rangle$ and α_A/α_M are temporal averages, where the averaging is started at time $t\Omega = 101$, a time Ω^{-1} after anisotropic viscosity is added to the system.

We show the evolution of the composite simulations in Figure 6, using four different Re with fixed Prandtl number $Pm = 1$. The $Re = 750, 3000, 10500$ simulations were performed at resolution $384 \times 192 \times 96$, while for $Re = 21000$ we went up in resolution to $768 \times 384 \times 192$. We checked that our $384 \times 192 \times 96$ simulations are converged by also running $Re = 10500$ at resolution $576 \times 288 \times 144$. Figure 6a shows the evolution of the box-averaged pressure anisotropy; the anisotropic stress evolution is given in Figure 6b. The evolution of the anisotropic heating fraction D_{μ_B}/D is shown in Figure 6c. The dashed vertical line indicates the time when MHD snapshots were restarted using Braginskii MHD with $Re_B = 0.75$. The MHD Δp , α_A and D_{μ_B}/D are computed from the MHD flow fields using the same μ_B that is used for the Braginskii runs, even though Δp is not dynamically present in MHD.

The rapid changes in Δp , α_A , D_{μ_B}/D and subsequent plateau are a convincing demonstration that we reach the Braginskii state very quickly. What is driving the abrupt transition? To understand this, it is instructive to look at $4\pi\Delta p/B^2$ snapshots, before and after anisotropic viscosity is introduced. The upper panels of Figure 7 show this for the $Re = Re_M = 21000$ simulation. In the MHD snapshot in Figure 7a, the vast majority of cells are pinned at the mirror/firehose limit. Moreover, there are many “opposite” cells in close proximity of each other. In these regions anisotropic viscosity operates on a short timescale, trying to eliminate the strong gradients. Doing so produces the smoother distribution of Δp depicted in Figure 7b and causes a rapid change in the volume-averaged Δp . The jump is less pro-

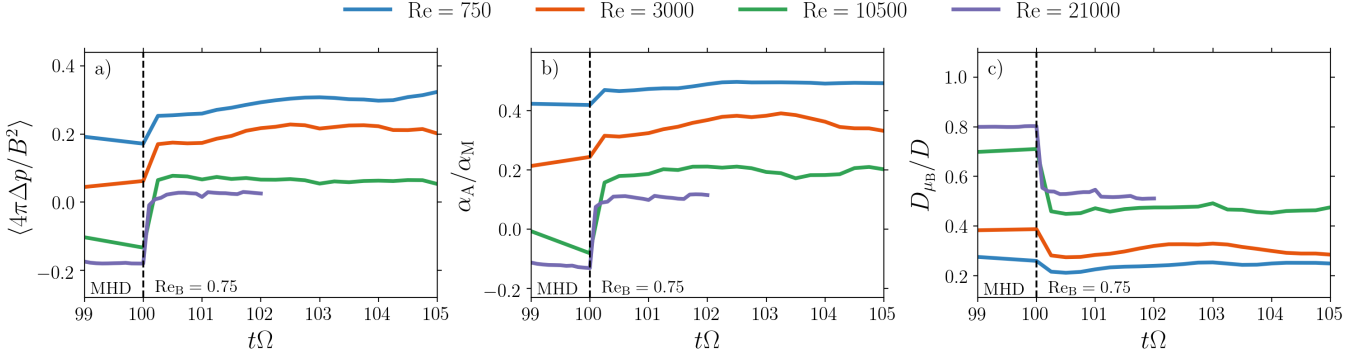


Figure 6. Evolution of a) anisotropic pressure, b) the ratio of anisotropic to Maxwell stress and c) the anisotropic viscous heating fraction in the composite MHD–Braginskii MHD simulations. The MHD turbulent flow field is restarted using Braginskii MHD with $\text{Re}_B = 0.75$ at $t\Omega = 100$ (prior to this time Δp , α_A and D_{μ_B}/D are calculated using the MHD flow field with $\text{Re}_B = 0.75$ even though μ_B is not dynamically present in the MHD equations). Each color represents a different choice of isotropic Reynolds number with fixed $\text{Pm} = 1$. Anisotropic pressure and anisotropic transport decrease with increasing Re . Meanwhile, anisotropic viscous heating increases with increasing Reynolds numbers, accounting for $\gtrsim 50\%$ of the total heating at large Re .

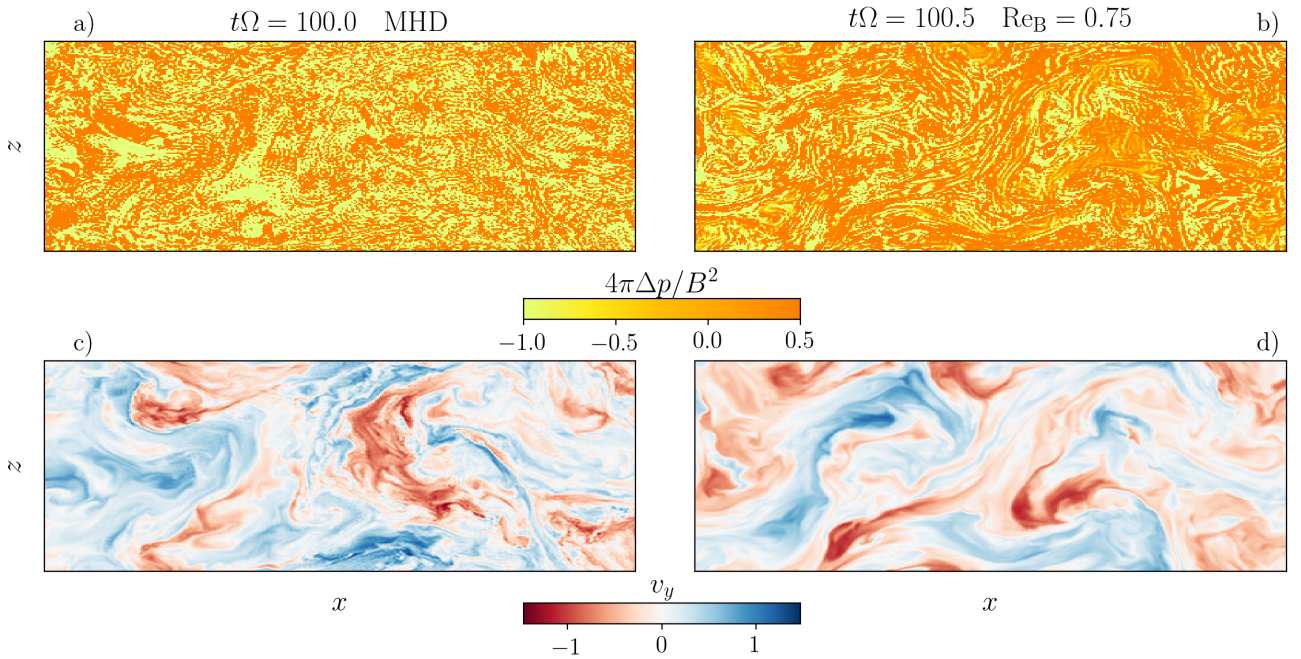


Figure 7. Snapshots from the composite simulation with $\text{Re} = 21000$ and $\text{Pm} = 1$. **Top:** snapshots of $\langle 4\pi\Delta p/B^2 \rangle$, before (left) and after (right) the MHD flow field is restarted using Braginskii MHD with $\text{Re}_B = 0.75$ (the MHD Δp is calculated using the MHD flow field with $\text{Re}_B = 0.75$, even though μ_B is not present in the MHD equations). Most cells are pinned at the hard-wall limits, with numerous mirror-firehose neighboring cells in the MHD snapshot. These small-scale variations are smoothed by anisotropic pressure in the right panel. **Bottom:** smoothing of MHD small-scale velocity variations (left) after Braginskii viscosity is introduced (right).

nounced at low Re , because the MHD flow field has already been smoothed by isotropic dissipation, thus diminishing the dynamical importance of anisotropic viscosity. In the bottom panels of Figure 7 we show how in the process of changing the statistics of Δp , Braginskii viscosity also reduces small-scale gradients in the velocity field.

The damping of high- k modes in the Braginskii velocity field leaves an imprint on the power spectrum. We show the kinetic and magnetic energy spectra of the composite sim-

ulation with $\text{Re} = 21000$, $\text{Pm} = 1$ in Figure 8, both for the MHD part and the Braginskii MHD ($\text{Re}_B = 0.75$) part of the run. Figure 8a shows that the kinetic-energy spectra in both models have spectral slopes close to $k^{-3/2}$, the MHD case being slightly shallower. There is also extra suppression of high- k velocity fluctuations in the Braginskii case, which is consistent with the snapshot in Figure 7d. Figure 8b demonstrates that the magnetic-energy spectra are hardly modified in Braginskii MHD.

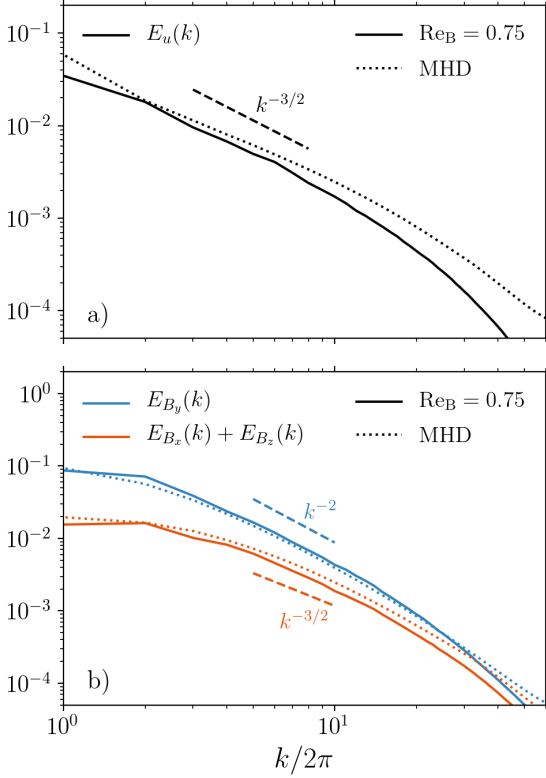


Figure 8. Energy spectra for the composite simulation with $\text{Re} = 21000$ and $\text{Pm} = 1$. The MHD part of the run ($t\Omega < 100$) is shown using dotted lines, while the Braginskii MHD part ($t\Omega > 101$) with $\text{Re}_B = 0.75$ is shown as solid lines. **Panel a):** Braginskii MHD has a velocity-field spectral slope close to $-3/2$, which is slightly steeper than the corresponding MHD slope. There is extra damping of high- k velocity fluctuations in the Braginskii case, due to the diffusive nature of the pressure anisotropy. **Panel b):** Magnetic-energy spectra are not strongly affected by the presence of anisotropic viscosity and look very similar in MHD and Braginskii MHD.

3.2.3 Dependence on Re and Re_M : magneto-immutable turbulence

In Figure 9a we show the pre-limiter anisotropic pressure distribution, before (MHD, dotted line) and after (solid line) the transition. Braginskii viscosity drives more cells into the region inside of the microinstability limits (dashed vertical lines), while damping the tails of the distribution (note that it is the *projection* of $\nabla \mathbf{u}$ onto the magnetic-field direction, $\hat{\mathbf{b}}\hat{\mathbf{b}} : \nabla \mathbf{u}$, that is strongly modified by anisotropic viscosity, $\hat{\mathbf{b}}\hat{\mathbf{b}}$ and $\nabla \mathbf{u}$ alone are only mildly affected). In addition, Figure 9a clearly shows that at low Re we get a distribution that is heavily skewed towards positive $\hat{\mathbf{b}}\hat{\mathbf{b}} : \nabla \mathbf{u}$. At higher Re , the distribution becomes more symmetric, leading to a smaller average pressure anisotropy, which explains the results in Figure 6.

The results in Figure 6 and Figure 9a can be explained qualitatively as follows. At low Re , high wavenumber modes of the flow field are efficiently damped by isotropic dissipation and so the fluctuating part of the $\hat{\mathbf{b}}\hat{\mathbf{b}} : \nabla \mathbf{u}$ distribution is narrow. Because the shear part of $\hat{\mathbf{b}}\hat{\mathbf{b}} : \nabla \mathbf{u}$ is strongly skewed towards positive values (since $\langle \hat{\mathbf{b}}\hat{\mathbf{b}} : \nabla \mathbf{u}_0 \rangle = \langle -\frac{3}{2} b_x b_y \Omega \rangle > 0$), the sum of the two is also going to be biased towards positive

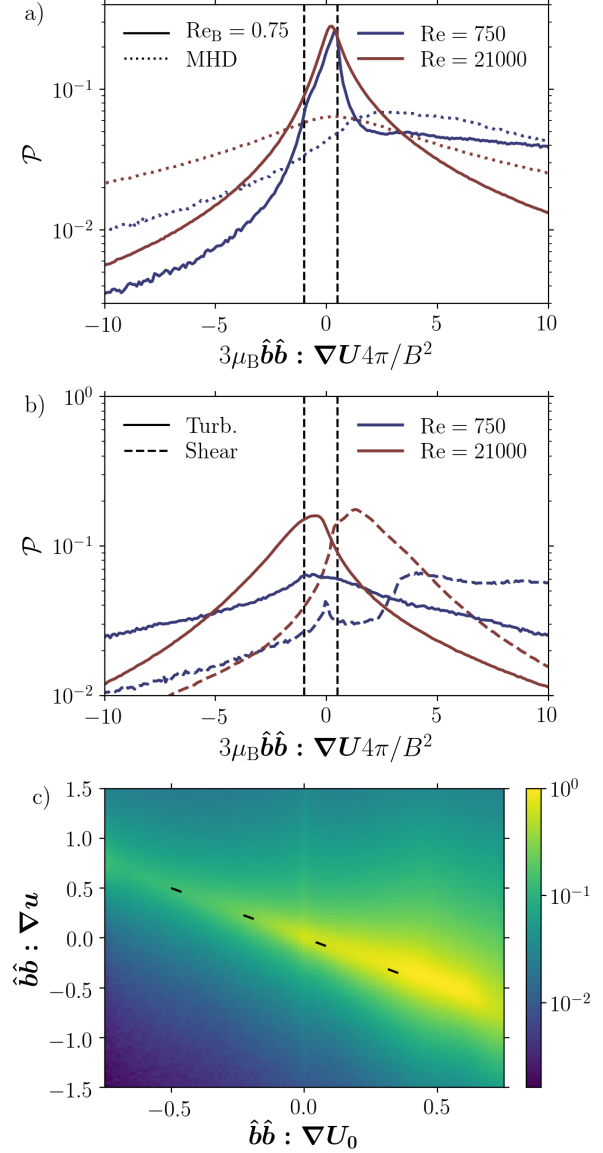


Figure 9. **Panel a):** impact of anisotropic viscosity and isotropic Reynolds numbers on the statistics of the pre-limiter $4\pi\Delta p/B^2$, i.e. $3\mu_B \hat{\mathbf{b}}\hat{\mathbf{b}} : \nabla \mathbf{U} 4\pi/B^2$, in the composite simulations with $\text{Re} = 750$, $\text{Re} = 21000$ (both with $\text{Pm} = 1$). The dotted lines are MHD at $t\Omega = 100$, the solid lines are Braginskii MHD with $\text{Re}_B = 0.75$ at time $t\Omega = 102$. Braginskii viscosity suppresses large $\hat{\mathbf{b}}\hat{\mathbf{b}} : \nabla \mathbf{u}$ gradients and drives more cells into the region between the dashed vertical lines (indicating the mirror and firehose limits). The distribution is more symmetric at higher isotropic Reynolds numbers, resulting in a smaller $\langle \Delta p \rangle$. **Panel b):** Contributions to $3\mu_B \hat{\mathbf{b}}\hat{\mathbf{b}} : \nabla \mathbf{U} 4\pi/B^2$ from the background shear \mathbf{U}_0 (dashed lines) and the turbulent fluctuations \mathbf{u} (solid lines) for $\text{Re} = 750$ and $\text{Re} = 21000$. Both simulations have $\text{Pm} = 1$ and $\text{Re}_B = 0.75$. At large Re , $\hat{\mathbf{b}}\hat{\mathbf{b}} : \nabla \mathbf{u}$ is less constrained by isotropic dissipation, so that anisotropic viscosity more effectively counteracts the positive shear contribution. This produces the more symmetric $3\mu_B \hat{\mathbf{b}}\hat{\mathbf{b}} : \nabla \mathbf{U} 4\pi/B^2$ distribution at large Re , shown in the top panel, with suppressed anisotropic transport (Figure 10). **Panel c):** 2D histogram of shear and turbulent contributions to $\hat{\mathbf{b}}\hat{\mathbf{b}} : \nabla \mathbf{u}$ for the simulation with $\text{Re} = 21000$, $\text{Pm} = 1$ and $\text{Re}_B = 0.75$. The dashes indicate the line $\hat{\mathbf{b}}\hat{\mathbf{b}} : \nabla \mathbf{u} = -\hat{\mathbf{b}}\hat{\mathbf{b}} : \nabla \mathbf{U}_0$. The anisotropic viscous stress causes the turbulent $\hat{\mathbf{b}}\hat{\mathbf{b}} : \nabla \mathbf{u}$ to balance the largely positive $\hat{\mathbf{b}}\hat{\mathbf{b}} : \nabla \mathbf{U}_0$ to resist field-line stretching and make the flow magneto-immutable (Squire et al. 2018).

values. This leads to a positive and appreciable Δp approaching the mirror threshold.

Increasing Re and Re_M means that there are higher wavenumber modes in the turbulent velocity field. In particular, note that $\nabla \mathbf{u} \sim k^{3/4}$ for a $k^{-3/2}$ spectrum (see Figure 8a), so it increases with increasing resolution. As a result, the fluctuating part of $\hat{\mathbf{b}}\hat{\mathbf{b}} : \nabla \mathbf{u}$ becomes more important and can drive more cells towards the firehose limit. Moreover, in Figure 9b we show that the $\hat{\mathbf{b}}\hat{\mathbf{b}} : \nabla \mathbf{u}$ distribution actually has a negative skew for large- Re turbulence in Braginskii MHD, so that it cancels to a large extent the positive $\hat{\mathbf{b}}\hat{\mathbf{b}} : \nabla \mathbf{u}_0$ from the mean shear.

Figure 9c offers insight into the physics behind the negative skew of the $\hat{\mathbf{b}}\hat{\mathbf{b}} : \nabla \mathbf{u}$ distribution. The 2D histogram shows how in the $\text{Re} = 21000$, $\text{Re}_B = 0.75$ simulation the plasma rearranges itself to produce a $\hat{\mathbf{b}}\hat{\mathbf{b}} : \nabla \mathbf{u}$ that locally balances the shear. The fact that the turbulence counters the largely positive $\hat{\mathbf{b}}\hat{\mathbf{b}} : \nabla \mathbf{u}_0$ can be attributed to anisotropic viscosity causing the rearrangement of the flow field so as to resist changes in \mathbf{B} by minimizing $\hat{\mathbf{b}}\hat{\mathbf{b}} : \nabla \mathbf{u}$ (Squire et al. 2018). We interpret the results of Figure 9 as a consequence of this magneto-immutability: the turbulence can more effectively cancel the field-line stretching of the mean shear ($\hat{\mathbf{b}}\hat{\mathbf{b}} : \nabla \mathbf{u}_0$) at large Re , when the plasma is less constrained by isotropic dissipation. Anisotropic viscosity does also rearrange the turbulence at low Re and $\hat{\mathbf{b}}\hat{\mathbf{b}} : \nabla \mathbf{u}$ is able to locally cancel $\hat{\mathbf{b}}\hat{\mathbf{b}} : \nabla \mathbf{u}_0$ to an appreciable extent (see Figure 9a for $\text{Re} = 750$), but the effect is more pronounced at high Re .

As the $\hat{\mathbf{b}}\hat{\mathbf{b}} : \nabla \mathbf{u}$ distribution becomes broader and more symmetric with increasing Re , comparable numbers of cells land on the mirror and firehose sides. As a result, $\langle 4\pi\Delta p/B^2 \rangle$ and α_A/α_M decrease in value, as in Figure 6. α_A/α_M can nevertheless remain more positive in comparison, primarily due to $\langle -B_x B_y \rangle$ typically being larger when averaged over cells at the mirror limit than cells at the firehose limit. It is not entirely surprising that the Maxwell stress is different at the two microinstability boundaries. For example, where the Maxwell stress is negative, the mean shear drives cells towards the firehose side (as $\hat{\mathbf{b}}\hat{\mathbf{b}} : \nabla \mathbf{u}_0 < 0$), whereas $\hat{\mathbf{b}}\hat{\mathbf{b}} : \nabla \mathbf{u}_0$ is skewed towards the mirror side where $-B_x B_y > 0$. The microinstabilities also significantly affect the dynamical effects of the Maxwell stress: at the firehose limit there is effectively no magnetic tension, and the Maxwell and anisotropic stresses cancel, while at the mirror boundary the effective magnetic tension is enhanced by a factor $(1 + 4\pi\Delta p/B^2)$.

The values of $\langle 4\pi\Delta p/B^2 \rangle$ and α_A/α_M as a function of isotropic Reynolds number are plotted in Figure 10a and Figure 10b respectively. In addition to $\langle 4\pi\Delta p/B^2 \rangle$, Figure 10a also shows the values of $4\pi\langle \Delta p \rangle / \langle B^2 \rangle$ as filled semi-transparent diamonds to demonstrate that the exact choice of averaging does not affect our conclusions. We show all our simulations with $\text{Pm} = 1$, which includes both full Braginskii (black) and composite MHD–Braginskii MHD simulations (red). The two procedures give consistent results in the shared range of Re , which supports the plausibility of composite simulation predictions at large Reynolds numbers (see also Appendix B).

Figure 10 shows that anisotropic transport and anisotropic pressure decrease significantly as we go to higher

Re and Re_M ¹. It remains unclear how they will behave as we let Re , $\text{Re}_M \rightarrow \infty$. Unfortunately probing larger isotropic Reynolds numbers is beyond our current computational capabilities.

In spite of $4\pi\langle \Delta p \rangle / \langle B^2 \rangle$, $\langle 4\pi\Delta p/B^2 \rangle \rightarrow 0$ at large Re , anisotropic pressure is an important source of dissipation. This is because regions at the firehose and mirror boundaries contribute positively to the anisotropic viscous heating rate (eq. 19), as Δp and $\hat{\mathbf{b}}\hat{\mathbf{b}} : \nabla \mathbf{u}$ have the same sign (see eq. 4). In Figure 11a we show that anisotropic viscosity becomes the dominant source of dissipation at large Re , even though the volume-averaged pressure anisotropy is a steadily decreasing function of Re (Figure 10).

3.2.4 Simulations with hyperdiffusion

By increasing the range of scales over which viscosity and resistivity are negligible, simulations with isotropic diffusion replaced by fourth-order hyperviscosity ($\nu_4 \nabla^4 \mathbf{u}$) and hyperresistivity ($\eta_4 \nabla^4 \mathbf{B}$) provide an alternative, indirect way of probing larger effective isotropic Reynolds numbers that does not require higher resolutions. We therefore augment our $\text{Pm} = 1$ simulations with hyperdiffusion simulations with varying

$$\text{Re}_4 = SL_z^4/\nu_4. \quad (20)$$

All simulations have a hyper-Prandtl number equal to 1, i.e. $\nu_4 = \eta_4$, and we summarize them in Table 2.

We show the $\langle 4\pi\Delta p/B^2 \rangle$ and α_A/α_M of our simulations with hyperdiffusion in Figure 12. At small Re_4 , $\langle 4\pi\Delta p/B^2 \rangle$ and α_A/α_M follow a similar trend to that shown in Figure 10. For large Re_4 , we obtain a plateau-like shape, with $\langle 4\pi\Delta p/B^2 \rangle \sim 0$ and $\alpha_A/\alpha_M \sim 0.1$. The plateau is consistent with the $\text{Re} = 21000$, $\text{Pm} = 1$ simulation, which suggests that this may already be close to the asymptotic limit when Re , $\text{Re}_M \rightarrow \infty$.

In Figure 11b we show that anisotropic viscous heating also increases with decreasing isotropic hyperdiffusivities, accounting for more than 60% of the total dissipation in our largest- Re_4 simulations (hyperviscous and hyperresistive heating are calculated as $\nu_4 \int d^3\mathbf{x} \mathbf{u} \cdot \nabla^4 \mathbf{u}$ and $\eta_4/(4\pi) \int d^3\mathbf{x} \mathbf{B} \cdot \nabla^4 \mathbf{B}$ respectively).

We end this section by pointing the reader to Appendix A2, where we discuss significant increases in α_M and α_{Re} that happen soon after Braginskii viscosity is introduced in the simulations with $\text{Re}_4 = 1.5 \times 10^8$ and $\text{Re}_4 = 7.5 \times 10^8$. While the origin of the enhanced transport remains unknown, we suspect that it is a numerical effect that is specific to hyperdiffusion operators (possibly overemphasis of channel modes in the presence of Braginskii viscosity) because our high- Re second-order-diffusion simulations did not give any indications of similar behavior.

¹ The trend that α_A/α_M and $4\pi\langle \Delta p \rangle / \langle B^2 \rangle$ decrease with increasing Reynolds numbers also seems to be present in our two simulations without firehose limiter (see Table 1; note, however, that the two simulations have different Pm). Quite notably, in spite of a large negative pressure anisotropy in the simulation with $\text{Re} = 10500$ and $\text{Pm} = 1$, anisotropic viscous transport remains positive.

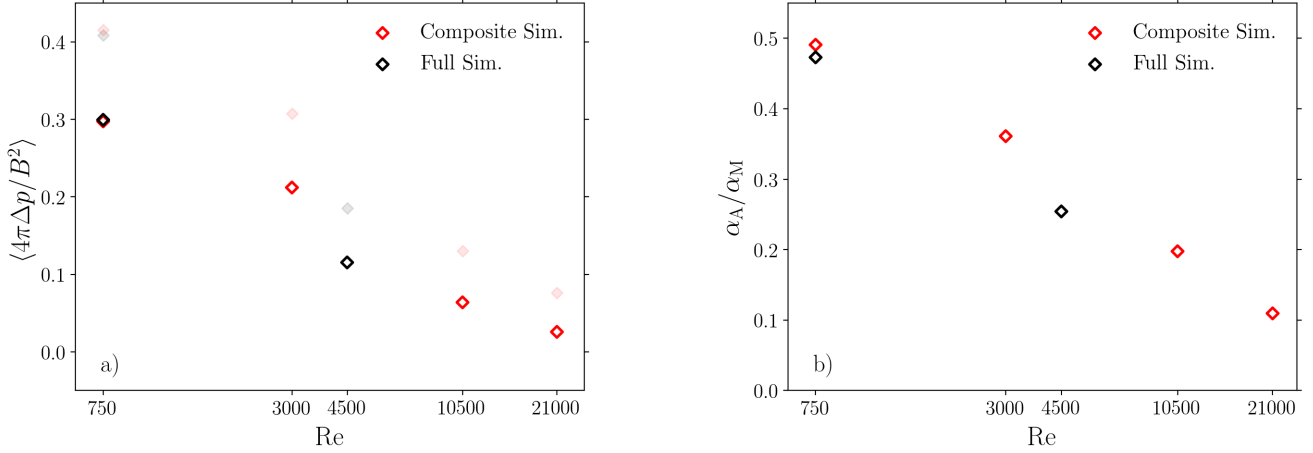


Figure 10. Anisotropic transport and anisotropic pressure vs. Re in simulations with $Pm = 1$ and $Re_B = 0.75$. **Panel a):** $\langle 4\pi\Delta p/B^2 \rangle$ for different isotropic Re . Also shown as filled semi-transparent diamonds are the corresponding values of $4\pi\langle\Delta p\rangle/\langle B^2 \rangle$. **Panel b):** ratio of anisotropic to Maxwell stress vs. Re . Composite (red) and full (black) simulations are in good agreement, showing that both anisotropic transport and anisotropic pressure decrease monotonically with isotropic Reynolds number.

Table 2. Summary of Braginskii MHD simulations with net vertical magnetic field and fourth-order isotropic hyperdiffusion. **Full** simulations were evolved for a time $t\Omega = 100$ and the values of $4\pi\langle\Delta p\rangle/\langle B^2 \rangle$, $\langle 4\pi\Delta p/B^2 \rangle$ and α_A/α_M are temporal averages over $t\Omega = 70 - 100$. In **Composite** simulations, MHD fields are restarted at $t\Omega = 100$ using Braginskii MHD. $4\pi\langle\Delta p\rangle/\langle B^2 \rangle$, $\langle 4\pi\Delta p/B^2 \rangle$ and α_A/α_M were averaged over $t\Omega = 101 - 110$, except for the $Re_4 = 7.5 \times 10^8$ simulation, for which the average is over $t\Omega = 101 - 102$.

Resolution	Sim. Type	Re_4	$Re_{M,4}$	ν_4/η_4	Re_B	$4\pi\langle\Delta p\rangle/\langle B^2 \rangle$	$\langle 4\pi\Delta p/B^2 \rangle$	α_A/α_M
(256, 128, 64)	Full	7.5×10^5	7.5×10^5	1	0.75	0.30	0.20	0.38
(256, 128, 64)	Composite	7.5×10^6	7.5×10^6	1	0.75	0.19	0.13	0.26
(256, 128, 64)	Full	3×10^7	3×10^7	1	0.75	0.071	0.026	0.13
(384, 192, 96)	Composite	1.5×10^8	1.5×10^8	1	0.75	0.069	0.012	0.13
(576, 288, 144)	Composite	7.5×10^8	7.5×10^8	1	0.75	0.034	-0.0096	0.085

4 OTHER FIELD CONFIGURATIONS

4.1 Net Toroidal and Vertical Field

In the previous section we have seen that transport properties in MHD and Braginskii MHD are remarkably similar, at least for the case of net vertical flux. Transport is modified primarily by the addition of anisotropic stress, but its importance decreases at large isotropic Re and Re_M . Anisotropic viscosity does significantly influence the heating of the plasma and the statistics of $\hat{\mathbf{b}}\hat{\mathbf{b}} : \nabla\mathbf{U}$, but it does not notably alter the turbulent amplitudes and transport properties of the flow.

In this section we look at a mixed vertical-azimuthal field geometry, which exhibits different linear behavior in Braginskii MHD and MHD, and so is arguably the most likely to show significant differences in nonlinear transport properties. More specifically, we use the field configuration,

$$\langle \mathbf{B} \rangle = B_0(\hat{\mathbf{y}} + \hat{\mathbf{z}}), \quad (21)$$

where B_0 is the same as in Section 3. In this field configuration with equal toroidal and vertical components, Quataert et al. (2002) and Balbus (2004) have shown that anisotropic pressure increases the linear growth rate of the MRI in Ke-

plerian discs from 0.75Ω to $\sqrt{3}\Omega$. Here we try to address whether there are any differences in the nonlinear dynamics.

We run our vertical-azimuthal-field simulations in boxes of size $L_x = 4$, $L_y = 4$ and $L_z = 1$, just like for the net-vertical-flux case described in Section 3. While in this field configuration the MRI modes are larger in scale, we have found that this box size is sufficient to capture the fastest-growing MRI wavelengths (Figure 13 supports this) and the fastest-growing parasitic modes (similar to the net-vertical-field case, horizontally narrow $1 \times 4 \times 1$ boxes did not correctly capture the most important parasitic modes).

First we focus on how the MRI enters the nonlinear growth phase. Figure 13 shows the evolution of the MRI in Braginskii MHD with $Re_B = 0.75$, as it transitions from linear growth to the nonlinear regime. In order for the growth rates to be close to the ideal values, we are using hyperdiffusion to dissipate energy just above the grid scale. The initial growth rate of $\langle B_x^2 \rangle$ is close to the theoretical value of $2\sqrt{3}\Omega$. Once the perturbed magnetic energy becomes comparable to the energy in the background field, the presence of anisotropic-pressure limiters becomes significant. This limits the dynamical importance of the anisotropic stress, which causes the growth rate to decrease to its MHD value and the

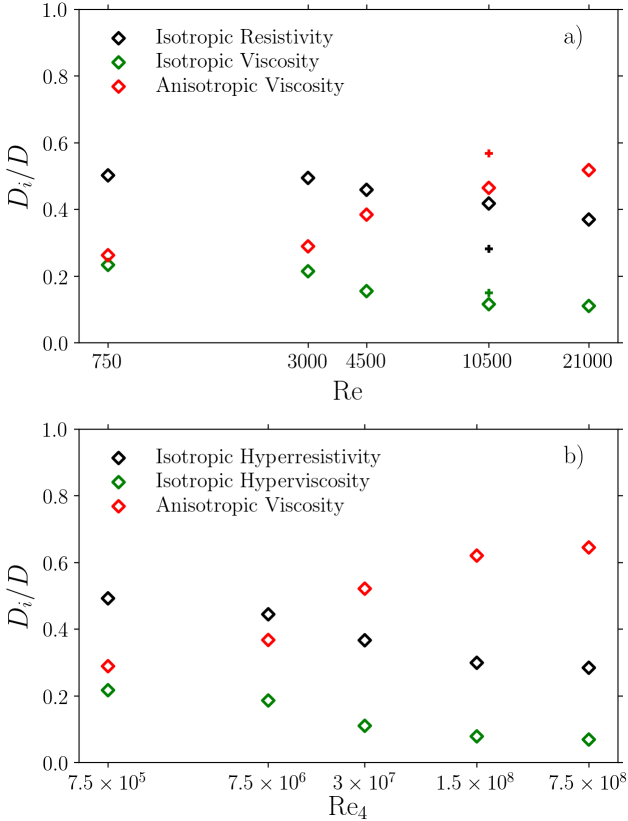


Figure 11. Panel a): temporal averages of heating fractions vs. Re for simulations with $Re_B = 0.75$, $Pm = 1$. Heating due to anisotropic viscosity becomes more significant at large isotropic Reynolds numbers, exceeding 50% of the total dissipation. This is also true in our $Re = 10500$, $Pm = 4$ simulation, which we show using “+” markers. **Panel b):** Same as the top panel, but for our simulations with hyperdiffusion (with $Re_4 = SL_z^4/\nu_4$), demonstrating that we get qualitatively similar behavior in simulations with hyperdiffusion.

fastest-growing mode to migrate to shorter wavelengths. See [Squire et al. \(2017a\)](#) for more discussion.

In Figure 14 we show the complete evolution into turbulence for $Re = 750$ and $Re = 4500$, both with $Pm = 1$. The evolution of α is shown in Figure 14a. The dotted line represents the MHD solution and the solid line is the $Re_B = 0.75$ evolution. Due to the faster linear growth phase, Braginskii MHD saturates into turbulence earlier, but the final turbulent state is again similar to the MHD solution.

We show the evolution of α_A/α_M in Figure 14b. We have chosen the same Re as in the full Braginskii simulations with net vertical field (see Figure 10). The result is qualitatively the same: α_A/α_M is smaller at large isotropic Reynolds numbers. Heating due to anisotropic viscosity (Figure 14c) nonetheless increases with increasing Re , which is consistent with our simulations with net vertical field. The temporal averages of α_A/α_M and D_{μ_B}/D obtained here are also very similar to the ones in Figure 10 and Table 1.

In addition to our $Pm = 1$ simulations, we have also evolved the $\langle B_y \rangle = \langle B_z \rangle$ field for other choices of Prandtl

number. For temporal averages of transport coefficients we refer the reader to Table 3.

Just like for the case of net vertical flux, we find that the total level of angular-momentum transport is not greatly affected by the presence of anisotropic pressure. The decrease in anisotropic transport at high Reynolds numbers, accompanied by increased anisotropic viscous heating, also persists in boxes threaded by equal vertical and azimuthal fields.

4.2 Zero Net Flux

In Section 3 we showed that the Prandtl-number dependence of ordinary MHD is recovered in Braginskii MHD with net vertical field. We now turn our attention to the zero-net-flux case, where there is no mean magnetic field threading the box. As is common in previous literature, we start from the initial condition

$$\mathbf{B}(t = 0) = B_0 \sin\left(\frac{2\pi x}{L_x}\right) \hat{\mathbf{z}}. \quad (22)$$

[Fromang et al. \(2007\)](#) showed that whether turbulence is sustained or decaying in zero-net-flux simulations is highly sensitive to the isotropic Reynolds and Prandtl numbers. Given the viscous nature of the pressure anisotropy, it is instructive to see if this behavior is modified in Braginskii MHD. More specifically, if anisotropic pressure were to modify the effective Prandtl number, we should see a clear imprint near the turbulence/no turbulence boundary.

Most of our zero-net-flux simulations are in boxes of dimensions $1 \times 4 \times 1$, which is similar to [Fromang et al. \(2007\)](#). We also ran a few simulations in horizontally extended boxes ($4 \times 4 \times 1$), although this does not significantly modify the bulk transport properties in the case of zero net flux (unlike magnetic-field geometries with a net vertical component). In both cases B_0 is chosen such that the initial average magnetic energy is the same as in the net-vertical-flux case described in Section 3.

Table 4 gives a summary of our zero-net-flux simulations. Once again, we do not find any systematic new behavior introduced by anisotropic viscosity. The time-averaged values of α may differ by order unity, but there does not seem to be a general trend.

In Figure 15 we show the turbulence/no turbulence boundary in $Re-Pm$ space, in MHD and in Braginskii MHD with $Re_B = 0.75$. This can be compared to Fig. 11 in [Fromang et al. \(2007\)](#), who show the analogous boundary for compressible MHD. In spite of the additional large anisotropic viscosity, the turbulence boundary is apparently unchanged in Braginskii MHD.

Figure 16 shows the evolution of angular-momentum transport in some of our zero-net-flux simulations. While the low-Prandtl-number simulation decays both in MHD and in Braginskii MHD, at high Prandtl number both models can sustain turbulence. The turbulence/no turbulence behavior does not change when Braginskii viscosity is present.

5 CONCLUSIONS

In this paper we have examined the importance of anisotropic pressure for MRI-driven turbulence in a shearing box. This was achieved through a combination of full

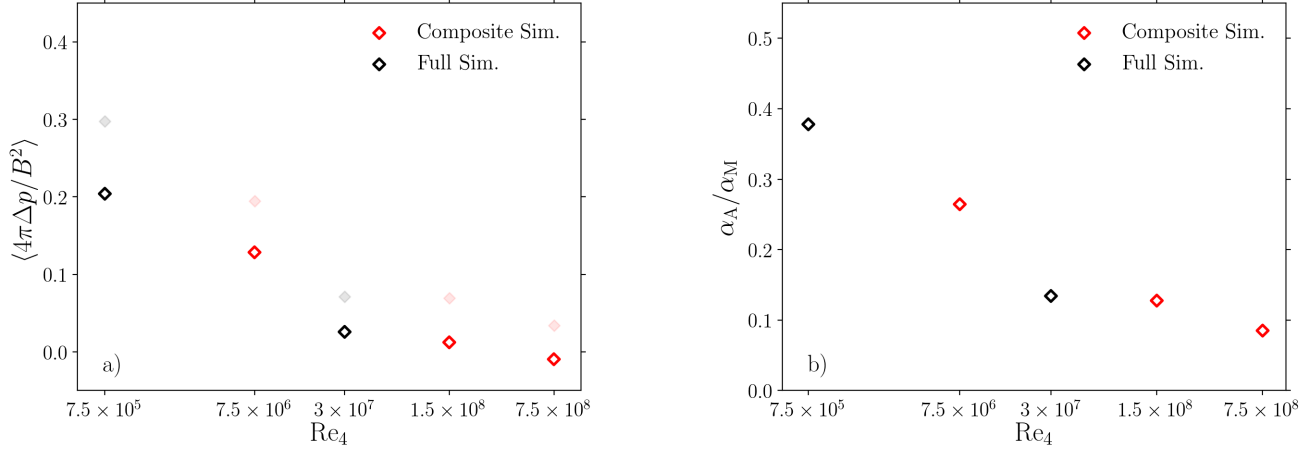


Figure 12. Same as Figure 10 but with fourth-order hyperdiffusion. As before, we show the values of $4\pi\langle\Delta p\rangle/\langle B^2\rangle$ in the left panel as filled semi-transparent diamonds. At small $Re_4 = SL_z^2/\nu_4$ we get a dependence qualitatively similar to second-order diffusion. At large Re_4 we obtain a plateau-like shape with $\langle 4\pi\Delta p/B^2 \rangle \sim 0$, $4\pi\langle\Delta p\rangle/\langle B^2 \rangle \sim 0$ and $\alpha_A/\alpha_M \sim 0.1$.

Table 3. Summary of simulations with net toroidal and vertical magnetic field ($\langle B_y \rangle = \langle B_z \rangle$). The transport coefficients and mean pressure anisotropies were averaged over $t\Omega = 100 - 200$.

Resolution	Re	Re _M	Pm	Re _B	α_{Re}	α_M	α_A	α	$4\pi\langle\Delta p\rangle/\langle B^2 \rangle$	$\langle 4\pi\Delta p/B^2 \rangle$	α_A/α_M
(256, 128, 64)	3000	1500	0.5	–	0.0056	0.022	–	0.028	–	–	–
(256, 128, 64)	3000	1500	0.5	0.75	0.0064	0.019	0.0076	0.033	0.32	0.24	0.40
(256, 128, 64)	750	750	1	–	0.0059	0.023	–	0.029	–	–	–
(256, 128, 64)	750	750	1	0.75	0.0064	0.020	0.0094	0.036	0.41	0.30	0.47
(256, 128, 64)	4500	4500	1	–	0.0067	0.033	–	0.040	–	–	–
(256, 128, 64)	4500	4500	1	0.75	0.011	0.042	0.011	0.063	0.18	0.11	0.25
(192, 96, 48)	750	3000	4	–	0.011	0.067	–	0.078	–	–	–
(192, 96, 48)	750	3000	4	0.3	0.014	0.063	0.022	0.099	0.28	0.19	0.36

incompressible Braginskii MHD simulations and composite MHD–Braginskii MHD simulations, in which fully turbulent MHD flow fields were restarted with Braginskii viscosity included, in order to minimize the computational cost due to the large viscosity (Appendix B validates this method). We find that bulk transport properties of MRI turbulence are effectively unchanged by large Braginskii viscosities. This is at first glance surprising given that the pressure-anisotropy stresses are at least as important as other forces in the system and modify the flow structures in the turbulence.

We looked at three initial magnetic-field orientations, including net vertical flux, equal net toroidal and vertical field, and zero net flux. All were examined using a number of isotropic Reynolds and magnetic Reynolds numbers. In our simulations, we augmented the Braginskii equations (1–4) to account for the presence of kinetic microinstabilities: the mirror and firehose instabilities, which are excited when the pressure anisotropy becomes comparable to the magnetic pressure (equations 5 & 6). As these instabilities tend to pin Δp near marginal stability (Kunz et al. 2016), we include

this kinetic result by introducing hard-wall limits on Δp in our fluid simulations at the instability thresholds.

We can divide our results into two main categories. Our first result concerns the level of angular-momentum transport in Braginskii MHD. We find that, for the range of isotropic diffusivities tested in this work, the Maxwell and Reynolds components of the stress tensor are hardly modified in Braginskii MHD. The presence of Braginskii viscosity modifies transport primarily through its additional anisotropic viscous stress component. This anisotropic viscous stress, however, is consistently smaller than the Maxwell stress, so that the total angular-momentum transport is only mildly affected.

One interesting consequence of this is that in Braginskii MHD transport remains very sensitive to isotropic diffusivities, despite the fact that the anisotropic viscosity is orders of magnitude larger than the isotropic viscosity. For the range of Reynolds numbers probed, the Maxwell and Reynolds stresses exhibit the same magnetic-Prandtl-number dependence as in ordinary MHD in all of the tested magnetic-field

Table 4. Summary of simulations with zero net flux. The transport coefficients and the mean pressure anisotropies were averaged over $t\Omega = 100 - 200$. The last column indicates whether turbulence could be sustained (“SD” means that the turbulence is slowly decaying). See Figure 16 for examples.

Box Size	Resolution	Re	Re _M	Pm	Re _B	α_{Re}	α_{M}	α_{A}	α	$\langle 4\pi\Delta p/B^2 \rangle$	$\alpha_{\text{A}}/\alpha_{\text{M}}$	Turb?
(4, 4, 1)	(256, 128, 64)	1500	12000	8	—	0.0020	0.015	—	0.017	—	—	Yes
(4, 4, 1)	(256, 128, 64)	1500	12000	8	1.5	0.0040	0.020	0.0078	0.032	0.17	0.39	Yes
(4, 4, 1)	(256, 128, 64)	6000	12000	2	—	—	—	—	—	—	—	SD
(4, 4, 1)	(256, 128, 64)	6000	12000	2	1.5	—	—	—	—	—	—	SD
(1, 4, 1)	(64, 128, 64)	750	6000	8	—	—	—	—	—	—	—	No
(1, 4, 1)	(64, 128, 64)	750	6000	8	0.75	—	—	—	—	—	—	No
(1, 4, 1)	(64, 128, 64)	1500	6000	4	—	—	—	—	—	—	—	No
(1, 4, 1)	(64, 128, 64)	1500	6000	4	0.75	—	—	—	—	—	—	No
(1, 4, 1)	(64, 128, 64)	1500	12000	8	—	0.0012	0.0091	—	0.010	—	—	Yes
(1, 4, 1)	(64, 128, 64)	1500	12000	8	0.75	0.0021	0.011	0.0047	0.017	0.21	0.45	Yes
(1, 4, 1)	(64, 128, 64)	3000	6000	2	—	—	—	—	—	—	—	No
(1, 4, 1)	(64, 128, 64)	3000	6000	2	0.75	—	—	—	—	—	—	No
(1, 4, 1)	(64, 128, 64)	3000	12000	4	—	0.0008	0.0054	—	0.0061	—	—	Yes
(1, 4, 1)	(64, 128, 64)	3000	12000	4	0.75	0.0002	0.0010	0.0005	0.0017	0.24	0.53	Yes

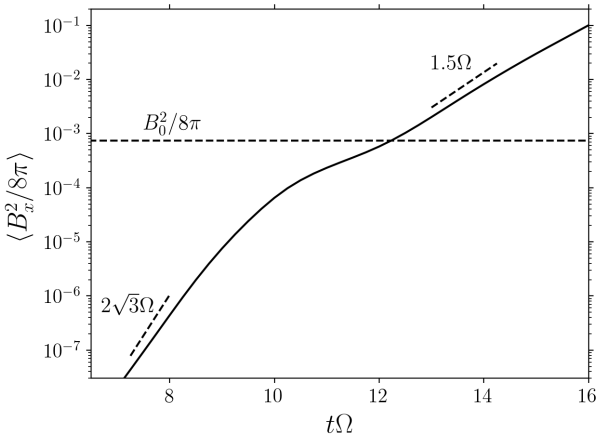


Figure 13. Linear and nonlinear evolution of the x-component of magnetic energy in Braginskii MHD with $\text{Re}_B = 0.75$ for $\langle B_y \rangle = \langle B_z \rangle$. In the linear phase the growth rate exceeds the MHD growth rate and agrees with the analytic prediction. In the nonlinear phase, when the pressure-anisotropy limiters become important, it reverts to the MHD growth rate.

configurations. This includes the temporal averages of α in net-flux simulations (see Figure 2), as well as the turbulence/no turbulence boundary in the $\text{Re} - \text{Pm}$ plane for zero-net-flux simulations (Figure 15). Remarkably, the angular-momentum transport in the shearing box, which is sensitive to a number of parameters (e.g. Pm , box size), appears to be almost unaffected by even large Braginskii viscosities.

Our systematic demonstration of MHD-like behavior in Braginskii MHD complements and clarifies some of the findings made by Sharma et al. (2006), Kunz et al. (2016), Squire et al. (2017a) and Foucart et al. (2017), who have seen strong

similarities to MHD in their extended-MHD and kinetic simulations. Nevertheless, we do find that anisotropic viscosity leaves a clear imprint on the structure of the flow. Δp is an important source of dissipation (Figure 11) and strongly modifies the velocity component along the local magnetic field (Figure 9). Surprisingly, this turns out to not significantly affect angular-momentum transport.

Our second primary result is related to the anisotropic viscous stress component. We have demonstrated that anisotropic transport becomes independent of anisotropic viscosity at sufficiently large anisotropic viscosity μ_B (see Figure 4), but is still sensitive to the amount of isotropic dissipation. This dependence is rather significant. We recover the typical result found in previous works – that $\alpha_A \sim \alpha_M$ – only at low isotropic Reynolds numbers. We find that the ratio α_A/α_M decreases systematically with Re and Re_M , down to ~ 0.1 for $\text{Re} = \text{Re}_M = 21000$. This is driven primarily by a decreasing average pressure anisotropy, as shown in Figure 10. Simulations with viscosity and resistivity replaced by hyperdiffusion operators suggest that $\alpha_A/\alpha_M \sim 0.1$ and $4\pi\langle\Delta p\rangle/\langle B^2\rangle, \langle 4\pi\Delta p/B^2\rangle \sim 0$ may be close to the asymptotic limit as $\text{Re}, \text{Re}_M \rightarrow \infty$ (see Figure 12). This has not been seen in any previous studies, which have consistently found an anisotropic stress that is comparable to the Maxwell stress (Sharma et al. 2006; Kunz et al. 2016; Foucart et al. 2017). However, previous fluid simulations with anisotropic pressure were at lower resolution and were grid-based rather than spectral, so it is likely that they correspond to our low- Re simulations. Although high resolutions were used in the fully kinetic simulations of Kunz et al. (2016), it is unclear whether the different α_A/α_M seen in this case arises from differences between weakly collisional and collisionless plasmas, or the difficulty of maintaining large scale separations

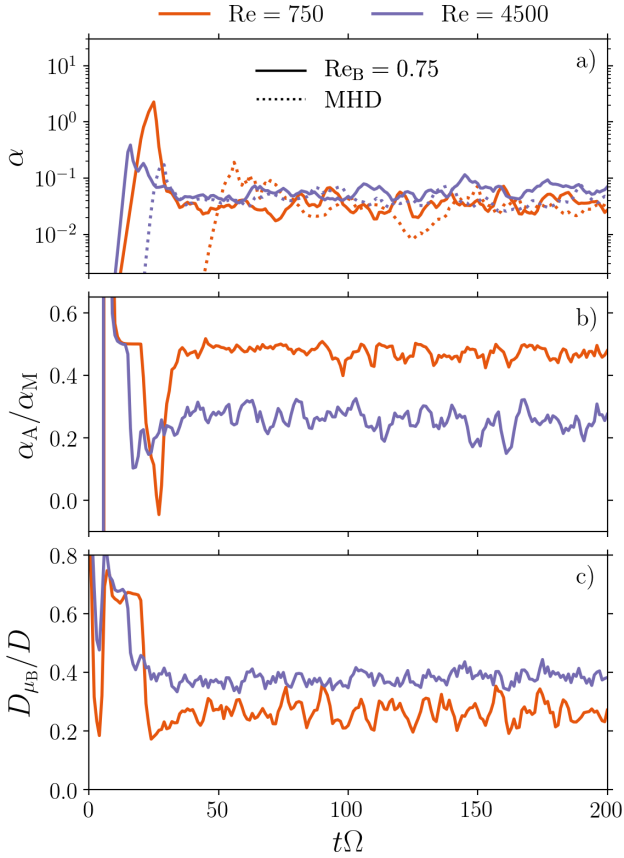


Figure 14. Evolution in a box with $\langle B_y \rangle = \langle B_z \rangle$ for $\text{Re} = 750$ and $\text{Re} = 4500$ (both with $\text{Pm} = 1$). **Panel a):** evolution of α in Braginskii MHD with $\text{Re}_B = 0.75$ (solid) and MHD (dotted). **Panel b):** evolution of α_A/α_M in Braginskii MHD for the two Re , again demonstrating that anisotropic transport is less significant at large Reynolds numbers. **Panel c):** evolution of the anisotropic viscous heating fraction in the two simulations. D_{μ_B}/D increases with increasing Re , which is consistent with our results for net vertical flux alone in Section 3 (Figure 11).

between the large-scale MRI-generated motions and plasma microinstabilities.

Even though $\langle 4\pi\Delta p/B^2 \rangle$ decreases with increasing Re , anisotropic pressure becomes a more important source of dissipation at large isotropic Reynolds numbers, accounting for more than 50% of the total heating at our highest Re . We show this in Figure 11.

We interpret the decreasing $\langle 4\pi\Delta p/B^2 \rangle$ and α_A/α_M with increasing Re as being due to the influence of isotropic dissipation on the statistics of $\hat{\mathbf{b}}\hat{\mathbf{b}} : \nabla\mathbf{U}$, thus affecting the box-averaged pressure anisotropy $\langle \Delta p \rangle$ via equation (4). Both the background shear \mathbf{U}_0 and the perturbed turbulent velocity field \mathbf{u} contribute to $\hat{\mathbf{b}}\hat{\mathbf{b}} : \nabla\mathbf{U}$. The background shear contribution, $\hat{\mathbf{b}}\hat{\mathbf{b}} : \nabla\mathbf{U}_0 = -\frac{3}{2}b_x b_y \Omega$, is largely positive. Meanwhile, $\hat{\mathbf{b}}\hat{\mathbf{b}} : \nabla\mathbf{u}$ is sensitive to the choice of Reynolds numbers. At low Re with more isotropic damping, the distribution of $\hat{\mathbf{b}}\hat{\mathbf{b}} : \nabla\mathbf{u}$ across the simulation domain is narrow, so that the mean shear leads to a skewed $\hat{\mathbf{b}}\hat{\mathbf{b}} : \nabla\mathbf{U}$ distribution with the vast majority of cells on the mirror side.

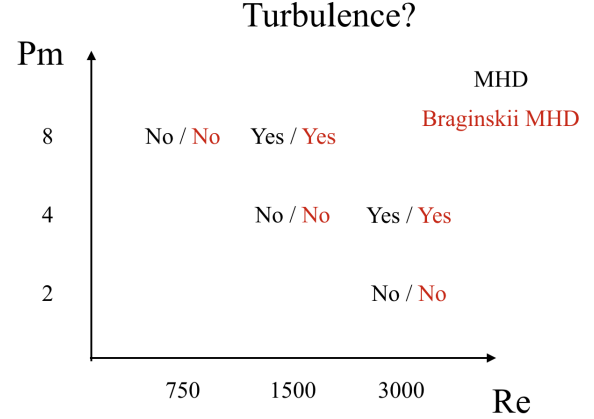


Figure 15. Zero-net-flux turbulence/no turbulence boundary in the $\text{Re} - \text{Pm}$ plane in MHD and Braginskii MHD with $\text{Re}_B = 0.75$. “No” means that turbulence eventually decayed; “Yes” indicates a Re , Pm pair where turbulence could be sustained. See Figure 16 for examples.

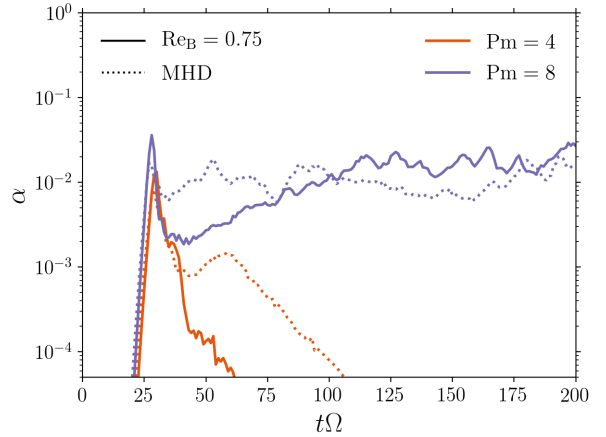


Figure 16. Evolution of α in a box with zero net flux, in MHD (dotted) and Braginskii MHD with $\text{Re}_B = 0.75$ (solid). We show the evolution for $\text{Re} = 1500$ with two different isotropic Prandtl numbers: $\text{Pm} = 4$ and $\text{Pm} = 8$. Like in MHD, low-Prandtl-number turbulence decays in Braginskii MHD and only high-Prandtl-number turbulence can be sustained.

This produces a large $\langle \Delta p \rangle$ close to the mirror threshold and $\alpha_A \sim \alpha_M$. In simulations with higher Re , $\hat{\mathbf{b}}\hat{\mathbf{b}} : \nabla\mathbf{u}$ is broader and more important, as higher wavenumber modes are present in the turbulent velocity field and $\nabla\mathbf{u} \sim k^{3/4}$ for a $k^{-3/2}$ spectral slope (see Figure 8a). The width of $\hat{\mathbf{b}}\hat{\mathbf{b}} : \nabla\mathbf{u}$ increases with increasing Re despite the large μ_B , as the damping of high- k modes in $\hat{\mathbf{b}}\hat{\mathbf{b}} : \nabla\mathbf{u}$ is significantly inhibited by the anisotropic-pressure limiters (since the highest- k modes typically correspond to unlimited $\Delta p \gg B^2/4\pi$, see Figure 9a). As a result, the fraction of cells with a negative Δp increases with increasing Re , which reduces the box-averaged pressure anisotropy. In addition, because the plasma is less constrained by isotropic dissipation at large Re , anisotropic viscosity can also more effectively reorganize the turbulence to balance the positive $\hat{\mathbf{b}}\hat{\mathbf{b}} : \nabla\mathbf{U}_0$ (shown in

Figure 9c). We interpret this as being related to the idea of magneto-immutability described in Squire et al. (2018), who show that anisotropic viscosity acts to minimize field-line stretching $\hat{\mathbf{b}}\hat{\mathbf{b}} : \nabla\mathbf{U}$ to resist changes in magnetic-field strength. For these reasons, high Re turbulence produces a more symmetric $3\mu_B\hat{\mathbf{b}}\hat{\mathbf{b}} : \nabla\mathbf{U}/B^2$ distribution centered closer to zero, and with comparable number of cells around the mirror and firehose limits (driven by the mean shear and turbulent fluctuations, respectively). This causes $\langle\Delta p\rangle$ and α_A to decrease with increasing Re. We illustrate this behavior in Figure 9, showing the distributions of $3\mu_B\hat{\mathbf{b}}\hat{\mathbf{b}} : \nabla\mathbf{U}4\pi/B^2$ for small and large Re.

Although $\langle 4\pi\Delta p/B^2 \rangle \rightarrow 0$ at large Re, the fractional heating due to anisotropic viscosity increases at large Re (Figure 11). This is because there is positive heating at both the firehose and mirror boundaries (since Δp and $\hat{\mathbf{b}}\hat{\mathbf{b}} : \nabla\mathbf{U}$ in eq. 19 have the same sign). Note also that $\langle|\Delta p|\rangle \sim \langle B^2/4\pi \rangle$ and $\langle|\hat{\mathbf{b}}\hat{\mathbf{b}} : \nabla\mathbf{U}|\rangle$ both increase with increasing Re.

While our simulations offered some insight, we must nonetheless still speculate about what happens when $\text{Re}, \text{Re}_M \rightarrow \infty$. Can α_A and $\langle\Delta p\rangle$ become negative? Or do they perhaps both tend to 0? Both cases would have interesting consequences, the latter implying that $\alpha_{\text{Braginskii}} \approx \alpha_{\text{Re}} + \alpha_M \rightarrow \alpha_{\text{MHD}}$, provided the Braginskii Maxwell and Reynolds stresses continue to track the MHD result (which is not entirely certain, see e.g. Appendix A2). Our simulations with hyperdiffusion tentatively suggest that $4\pi\langle\Delta p\rangle/\langle B^2 \rangle$, $\langle 4\pi\Delta p/B^2 \rangle \sim 0$ and $\alpha_A/\alpha_M \sim 0 \leftrightarrow 0.1$ are potential candidates for the asymptotic values. Nevertheless, exploring the asymptotic limit of large Reynolds numbers in detail is beyond the scope of this paper and a potential direction for future studies. This, however, would most likely require a more efficient Braginskii viscosity implementation than the one used in this work. Another interesting extension to this work would be to examine the compressible Braginskii MHD equations, including the effects of anisotropic conduction.

It is unclear if and how our results apply to a fully kinetic calculation. We have attempted to model some of the relevant microphysics by applying hard-wall limits on the pressure anisotropy. This subgrid model is intended to mimic how the mirror and firehose instabilities affect the pressure anisotropy. But it is unclear whether the limiters are a sufficient and/or accurate representation of the key microphysics. One can also speculate about the relevance of isotropic diffusivities in a collisionless system. Our results suggest that even collisionless-plasma-turbulence may be sensitive to isotropic dissipation. This, then, raises the question of what sets the isotropic diffusivities in a collisionless plasma, where transport properties generally depend on the Larmor radii of the plasma particles and kinetic microinstabilities that can readily modify the collisionality of the system. To understand this, fully kinetic particle-in-cell simulations are needed. However, such simulations are computationally expensive, and it is unclear whether the simulations can reach a sufficient dynamic range between the outer scale (e.g., disc rotation frequency) and microscopic plasma scales (e.g., the ion cyclotron frequency) to capture the fully developed turbulence that suppresses the pressure anisotropy and anisotropic transport in our simulations.

5.1 Implications for RIAFs

To conclude we briefly discuss some of the possible implications of our results for RIAFs, bearing in mind the caveat that it is not yet fully clear how our weakly collisional results apply to collisionless plasmas. Our results support previous work concluding that low-collisionality accretion discs may be reasonably modeled using fluid approximations (e.g., Foucart et al. 2017). Indeed, in some ways our results strengthen this conclusion by showing that the transport in a weakly collisional plasma is more similar to MHD when MRI-driven turbulence is well resolved. The primary difference relative to MHD in our simulations is that anisotropic viscous heating is a major ($\gtrsim 50\%$ at high Re; see Figure 11) source of heating and must be accounted for when modeling the plasma thermodynamics. Electron heating by anisotropic viscosity (e.g., Sharma et al. 2007) is thus a key ingredient for models that separately evolve the electron thermodynamics in order to model the radiation from RIAFs (e.g., Ressler et al. 2017; Chael et al. 2018). However, previous estimates of electron vs. proton heating by anisotropic viscosity (e.g., Sharma et al. 2007) assumed that the electron (proton) pressure anisotropy was near the electron whistler (mirror) threshold. This was motivated by the fact that the mean shear drives $\Delta p > 0$ (Figure 9b). However, we have shown that the turbulent fluctuations largely counteract the mean shear (Figure 9b) and thus viscous heating has significant contributions from both $\Delta p > 0$ and $\Delta p < 0$. This should be taken into account in future estimates of anisotropic viscous heating in RIAFs.

ACKNOWLEDGEMENTS

We thank C. Gammie, F. Foucart, A. Schekochihin and J. Stone for useful discussions, as well as all the members of the horizon collaboration, <http://horizon.astro.illinois.edu>, for their advice and encouragement. This work was supported in part by NSF grants AST 13-33612, AST 1715054, and a Simons Investigator award from the Simons Foundation. J.S. would like to acknowledge the support of a Rutherford Discovery Fellowship and the Marsden Fund, administered by the New Zealand Royal Society Te Apārangi. M.W.K. was supported by NASA grant NNX17AK63G. This work was also made possible by computing time granted by UCB on the Savio cluster.

REFERENCES

- Balbus S. A., 2004, *ApJ*, 616, 857
- Balbus S. A., Hawley J. F., 1991, *ApJ*, 376, 214
- Balbus S. A., Hawley J. F., 1998, *Rev. Mod. Phys.*, 70, 1
- Barnes A., 1966, *The Physics of Fluids*, 9, 1483
- Bodo G., Mignone A., Cattaneo F., Rossi P., Ferrari A., 2008, *A&A*, 487, 1
- Braginskii S. I., 1965, *Rev. Plasma Phys.*, 1, 205
- Chael A., Rowan M., Narayan R., Johnson M., Sironi L., 2018, *MNRAS*, 478, 5209
- Chandrasekhar S., Kaufman A. N., Watson K. M., 1958, *Proc. R. Soc. London A*, 245, 435
- Chew C. F., Goldberger M. L., Low F. E., 1956, *Proc. R. Soc. London A*, 236, 112

- Foucart F., Chandra M., Gammie C. F., Quataert E., 2016, *MNRAS*, 456, 1332
- Foucart F., Chandra M., Gammie C. F., Quataert E., Tchekhovskoy A., 2017, *MNRAS*, 470, 2240
- Fromang S., Papaloizou J., Lesur G., Heinemann T., 2007, *A&A*, 476, 1123
- Goodman J., Xu G., 1994, *ApJ*, 432, 213
- Hasegawa A., 1969, *The Physics of Fluids*, 12, 2642
- Hawley J. F., Gammie C. F., Balbus S. A., 1995, *ApJ*, 440, 742
- Hawley J. F., Balbus S. A., Stone J. M., 2001, *ApJL*, 554, L49
- Hoshino M., 2015, *Phys. Rev. Lett.*, 114, 061101
- Inchingolo G., Grismayer T., Loureiro N. F., Fonseca R. A., Silva L. O., 2018, *ApJ*, 859, 149
- Kulsrud R. M., 1983, Residual energy in MHD turbulence and in the solar wind. In *MHD description of plasma Vol. 1* (ed. R N Sagdeev & M N Rosenbluth), p. 115
- Kunz M. W., Schekochihin A. A., Stone J. M., 2014, *Phys. Rev. Lett.*, 112, 205003
- Kunz M. W., Stone J. M., Quataert E., 2016, *Phys. Rev. Lett.*, 117, 235101
- Lesur G., Longaretti P. Y., 2007, *MNRAS*, 378, 1471
- Longaretti P. Y., Lesur G., 2010, *A&A*, 516, A51
- Mahadevan R., Quataert E., 1997, *ApJ*, 490, 605
- Mikhailovskii A. B., Tsypin V. S., 1971, *Plasma Physics*, 13, 785
- Parker E. N., 1958, *Phys. Rev.*, 109, 1874
- Pessah M. E., Goodman J., 2009, *ApJL*, 698, L72
- Quataert E., Dorland W., Hammett G. W., 2002, *ApJ*, 577, 524
- Ressler S. M., Tchekhovskoy A., Quataert E., Gammie C. F., 2017, *MNRAS*, 467, 3604
- Riquelme M. A., Quataert E., Verscharen D., 2015, *ApJ*, 800, 27
- Rosenbluth M. N., 1956, Los Alamos Sci. Lab. Rep., LA-2030
- Schekochihin A. A., Cowley S. C., Kulsrud R. M., Rosin M. S., Heinemann T., 2008, *Phys. Rev. Lett.*, 100, 081301
- Schekochihin A. A., Cowley S. C., Rincon F., Rosin M. S., 2010, *MNRAS*, 405, 291
- Sharma P., Hammett G. W., Quataert E., Stone J. M., 2006, *ApJ*, 637, 952
- Sharma P., Quataert E., Hammett G. W., Stone J. M., 2007, *ApJ*, 667, 714
- Sironi L., Narayan R., 2015, *ApJ*, 800, 88
- Squire J., Quataert E., Schekochihin A. A., 2016, *ApJL*, 830, L25
- Squire J., Quataert E., Kunz M. W., 2017a, *Journal of Plasma Physics*, 83, 905830613
- Squire J., Kunz M. W., Quataert E., Schekochihin A. A., 2017b, *Phys. Rev. Lett.*, 119, 155101
- Squire J., Schekochihin A. A., Quataert E., Kunz M. W., 2018, preprint ([arXiv:1811.12421](https://arxiv.org/abs/1811.12421))

APPENDIX A: ENHANCED TRANSPORT IN BRAGINSKII MHD

A1 Dependence on box aspect ratio

The most notable departure from MHD behavior came about when testing different box aspect ratios for domains with a net vertical field. In addition to our standard $4 \times 4 \times 1$ boxes, we also looked at narrower domains with aspect ratios $1 \times 4 \times 1$ and $1 \times \pi \times 1$. Consistent with Bodo et al. (2008), Pessah & Goodman (2009) and Longaretti & Lesur (2010), we have also found that MHD simulations in boxes with $L_x : L_z = 1$ and net vertical field show stronger fluctuations with recurring bursts. This has been attributed to such boxes not capturing the fastest growing parasitic modes and overemphasizing the role of channel modes.

While we discovered no surprising behavior in MHD, anisotropic viscosity produced some surprising results. $L_y =$

4 still showed fairly comparable turbulence in MHD and Braginskii MHD, but this was no longer the case for $L_y = \pi$. As the box becomes narrow enough, e.g. $1 \times \pi \times 1$, the presence of anisotropic viscosity strongly enhances transport, with α increasing monotonically with μ_B . Both the turbulent energy densities and transport can increase by orders of magnitude for large μ_B . A natural interpretation is that a high anisotropic viscosity causes some parasitic modes to migrate to longer wavelengths. These are not captured by our narrow boxes, thus allowing MRI modes to drive turbulence at a larger amplitude. For boxes with $4 \times 4 \times 1$, this is no longer the case. Another plausible explanation is that anisotropic viscosity decreases the growth rate of short-wavelength modes and so wider boxes are needed to accommodate long-wavelength modes.

A2 Braginskii MHD with isotropic hyperdiffusion

Our composite MHD–Braginskii MHD simulations with small hyperdiffusion ($\text{Re}_4 = 1.5 \times 10^8$ and $\text{Re}_4 = 7.5 \times 10^8$) show significant increases in the Maxwell and Reynolds stresses almost immediately after Braginskii viscosity is introduced ($\alpha_A/\alpha_M \sim 0.1$ stays at a roughly constant level nevertheless, as in Figure 12). For example, in the simulation with $\text{Re}_4 = 1.5 \times 10^8$, in which the Braginskii MHD part could be evolved for longer ($t\Omega = 100 - 130$), α_M increases by a factor of a few. There are signs of burst-like behavior, suggesting that it may be related to impeded disruption of channel modes in simulations with hyperdiffusion and Braginskii viscosity. Unfortunately, the large anisotropic viscosity and high resolutions at which this behavior occurs prohibit us from thoroughly testing the origin of the increased transport. Thus, it is unclear to what extent this is a physical effect and not simply a numerical artifact associated with our use of hyperdiffusion operators. This result should therefore be treated with caution, especially since we did not see any clear indications of strongly modified α_M or α_{Re} in our high-Re, second-order-diffusion simulations.

APPENDIX B: TEST CASE FOR RESTARTING MHD FLOW FIELD WITH BRAGINSKII VISCOSITY

In section 3.2 we use composite MHD–Braginskii MHD simulations to explore the behavior of anisotropic pressure and stress in the large Reynolds number regime at high resolution. We claimed that by restarting MHD flow fields with anisotropic viscosity, we are able to recover the appropriate Braginskii $\langle \Delta p \rangle$ in a fraction of an orbital period. This allowed us to determine the anisotropic stress at high Reynolds numbers, which would otherwise be numerically prohibitive with our current methods. Here we justify our “restart” method by looking at one of our fully evolved Braginskii MHD simulations.

We focus on the case $\text{Re} = 6000$, $\text{Pm} = 0.5$ and $\text{Re}_B = 0.75$. It was evolved for a time $t\Omega = 200$ both in MHD and in Braginskii MHD. In Figure B1 we show the evolution of $\langle 4\pi\Delta p/B^2 \rangle$ and α_A/α_M for the two models. Once again, the pressure anisotropy computed from the MHD flow fields uses the same μ_B as the corresponding Braginskii simulation. The

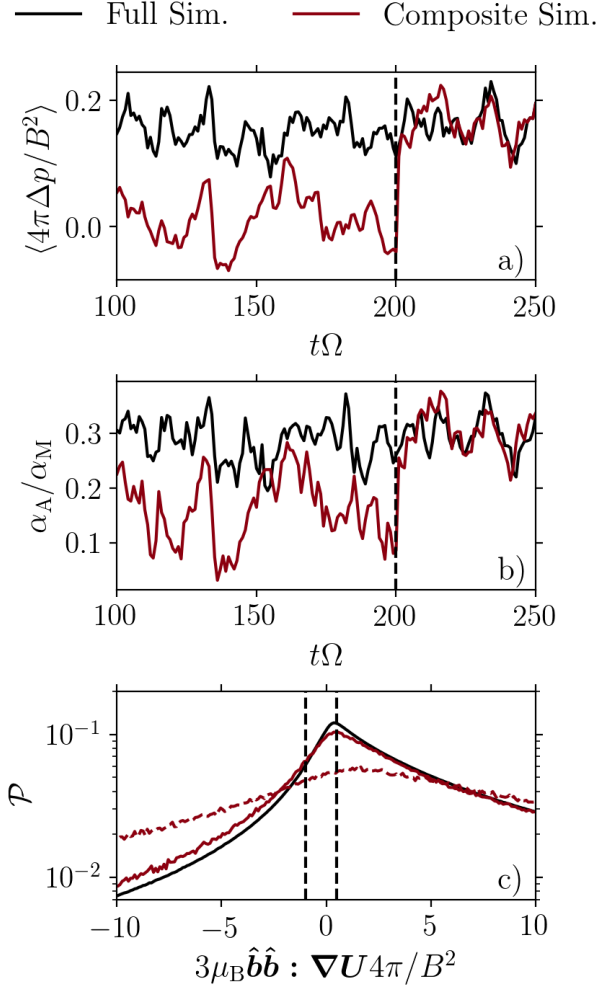


Figure B1. Test of composite MHD–Braginskii MHD simulations for the case $\text{Re} = 6000$, $\text{Pm} = 0.5$ and $\text{Re}_B = 0.75$. The black line represents the full Braginskii simulation, the crimson line is the composite simulation in which the MHD flow field is restarted with $\text{Re}_B = 0.75$ at $t\Omega = 200$. **Panel a):** evolution of $\langle 4\pi\Delta p/B^2 \rangle$. **Panel b):** evolution of α_A/α_M (prior to $t\Omega = 200$, Δp and α_A are calculated using the MHD flow field with $\text{Re}_B = 0.75$, even though μ_B is not present in the MHD equations). **Panel c):** distributions of $3\mu_B \hat{\mathbf{b}}\hat{\mathbf{b}} : \nabla \mathbf{U} 4\pi/B^2$. The black line is the distribution of the full Braginskii simulation averaged over $t\Omega = 100 - 200$. The dotted crimson line is the MHD distribution at time $t\Omega = 200$ and the solid crimson line is the distribution in the composite simulation at $t\Omega = 201$, after anisotropic viscosity was introduced. After the MHD flow field is restarted with anisotropic viscosity, the statistics of $3\mu_B \hat{\mathbf{b}}\hat{\mathbf{b}} : \nabla \mathbf{U} 4\pi/B^2$ and the evolution of $\langle 4\pi\Delta p/B^2 \rangle$ and α_A/α_M agree very well with the full Braginskii simulation.

plots show that the calculated Δp is quite different in Braginskii and ordinary MHD, the difference being more significant than the uncertainty related to temporal fluctuations.

The MHD-generated flow field is then restarted with anisotropic viscosity at time $t\Omega = 200$. This induces an almost immediate jump in Δp and α_A , which can be seen to reach values comparable to the full Braginskii simulation.

Afterwards, the two simulations show qualitatively identical evolutions of anisotropic stress and pressure.

Figure B1c shows how the restarting affects the pre-limiter Δp distribution. The dashed crimson line is the MHD distribution, immediately before the anisotropic viscosity is introduced at $t\Omega = 200$. The black line is the average distribution of the full Braginskii simulation. The solid crimson curve is the distribution generated by anisotropic viscosity by the time $t\Omega = 201$, so just one Ω^{-1} after the MHD field is restarted. The solid crimson and black curves are in very good agreement with one another, supporting our claim that anisotropic viscosity does not need much time to generate its desired $\hat{\mathbf{b}}\hat{\mathbf{b}} : \nabla \mathbf{U}$ distribution. This is not surprising given that the viscous time for μ_B in the vertical direction is $\sim \text{Re}_B \Omega^{-1} \sim \Omega^{-1}$.

This paper has been typeset from a T_EX/L^AT_EX file prepared by the author.